

A vertical rift in Saturn's inner C ring

Philip D. Nicholson^{a,*}, Matthew M. Hedman^b

^aDepartment of Astronomy, Cornell University, Ithaca NY 14853, United States

^bDepartment of Physics, University of Idaho, Moscow ID 83844, United States



ARTICLE INFO

Article history:

Received 17 June 2015

Revised 6 January 2016

Accepted 19 January 2016

Available online 3 February 2016

Keywords:

Occultations

Saturn, rings

Dynamics

ABSTRACT

In 1988 Rosen and Lissauer identified an unusual wavelike feature in Saturn's inner C ring as a bending wave driven by a nodal resonance with Titan (*Science* 241, 690). This is sometimes referred to as the –1:0 resonance since it occurs where the local nodal regression rate is approximately equal to $-n_T$, where $n_T = 22.577^\circ \text{ d}^{-1}$ is Titan's orbital mean motion. We have used a series of 44 stellar occultation profiles of this wave observed by the Cassini VIMS instrument to test their hypothesis. We find that, as predicted, this wave is an outward-propagating $m = 1$ spiral with a leading orientation and a retrograde pattern speed approximately equal to $-n_T$. But the most intriguing feature associated with the wave is a narrow gap that lies ~ 7 km outside the resonance. This gap varies noticeably in width and is seen in roughly 3/4 of the occultation profiles, appearing to rotate with the wave in a retrograde direction. We have developed a simple kinematical model that accounts for the observations and consists of a continuous but very narrow gap (radial width ≈ 0.6 km), the edges of which are vertically distorted by the propagating bending wave as it crosses the region. Differences in viewing geometry then largely account for the apparent width variations. We find vertical amplitudes of 3.8 km for the inner edge and 1.2 km for the outer edge in 2008, with nodes misaligned by $\sim 110^\circ$. Moreover, both edges of the gap are slightly eccentric, with pericenters aligned with Titan, suggesting that the eccentricities are forced by the nearby Titan apsidal resonance. We hypothesize that the gap forms because the local slopes in the bending wave become so great that nonlinear effects result in the physical disruption of the ring within its first wavelength, beyond which point the wave re-establishes itself with a reduced amplitude.

© 2016 Elsevier Inc. All rights reserved.

1. Introduction

The most prominent wave in Saturn's C ring is the Titan nodal bending wave, driven by the Titan –1:0 inner vertical resonance (IVR) and first described in *Voyager* radio occultation (RSS) data by Rosen and Lissauer (1988). At this resonance, the nodal regression rate of ring particles is equal in magnitude, but opposite in sign, to the mean motion of Titan. Because of its negative pattern speed (*i.e.*, the wave pattern rotates in the retrograde direction) this wave propagates radially outwards, unlike most bending waves, and is predicted to take the form of a 1-armed leading spiral. A curious feature of the *Voyager* RSS profile of the nodal bending wave is a 15 km wide gap in the inner part of the wave train, located at a radius of $\sim 77,530$ km. Rosen and Lissauer (1988) suggested that it was not a real gap, but an artifact of the very shallow incidence angle of the RSS occultation combined with the tilted surface of the ring due to the bending wave. Essentially, a region of ring whose surface normal is tilted towards the observer can appear much

lessopaque than its neighbors when the measured transmission is converted to normal optical depth using the standard formula. The gap's sharp edges, in this picture, were associated with multiple ray crossings through the warped ring. This unique feature, combined with some inconsistencies in the dynamical parameters for the wave implied by the analysis by Rosen and Lissauer (1988), led us to reexamine this region in the several dozen stellar occultation profiles obtained to date by the *Cassini* VIMS investigation.

We find that the gap, far from being unique to low-elevation angle occultations, appears in ~3/4 of the VIMS profiles, including many obtained at quite high elevation angles. In the VIMS data, however, it is at most 5 km wide, much narrower than in the *Voyager* RSS profile, and in ~1/4 of the VIMS profiles it disappears completely, only to be replaced by a local maximum in optical depth. Our investigation shows that the gap is in fact real, but that its edges are vertically distorted by the wave in which it is embedded: in effect it is a vertical “tear” in the rings more than a radial gap. Variations in the viewing geometry of the occultations lead to the large apparent variations in the gap's width, and even to its disappearance at some longitudes. The description of this novel feature, and its relationship to the nearby Titan –1:0 IVR and to

* Corresponding author. Tel.: +16072558543.

E-mail address: nicholso@astro.cornell.edu (P.D. Nicholson).

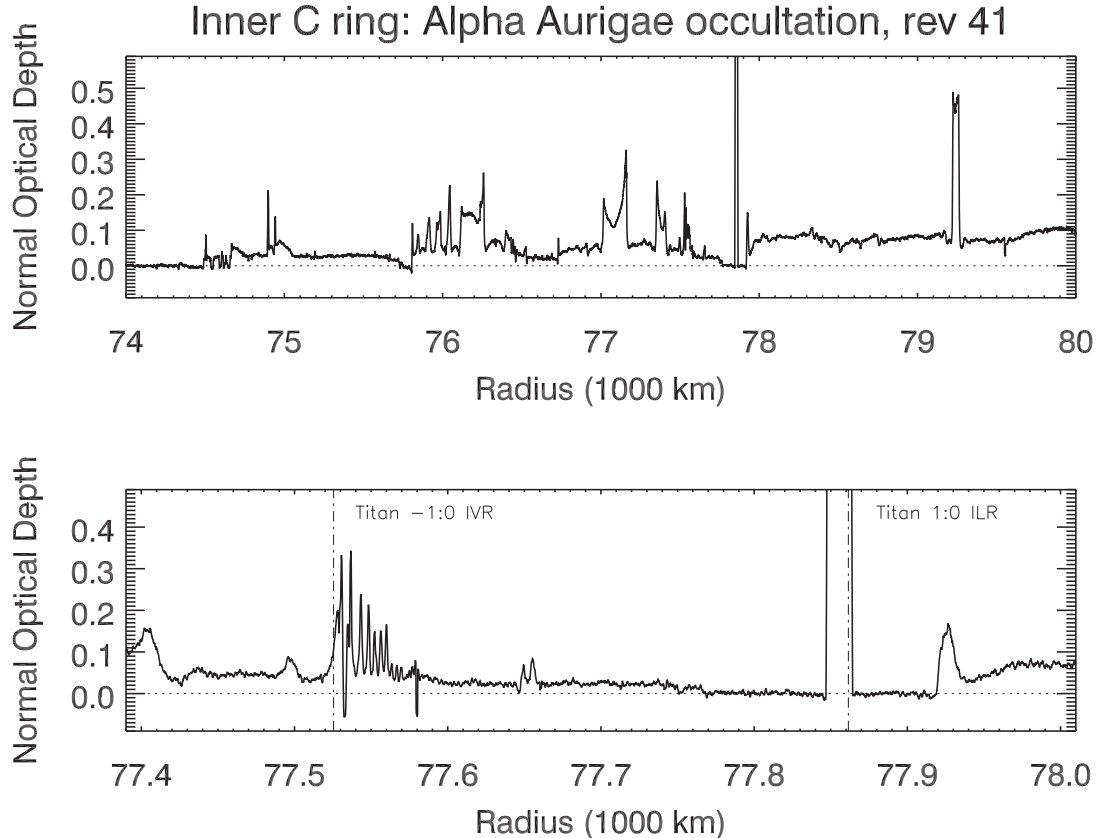


Fig. 1. An optical depth profile of the inner C ring derived from the VIMS α Aurigae occultation on the *Cassini* orbit designated Rev 41, showing the spatial context for the present study. The lower panel shows the region that contains the Titan ringlet and nodal bending wave at a scale expanded by a factor of 10, and a radial resolution of 2 km. The Titan apsidal (or 1:0) resonance falls within the Colombo gap at 77,862 km, where it controls the shape of the eccentric Titan ringlet, while the Titan nodal (or $-1:0$) resonance at 77,525 km drives the outward-propagating bending wave visible at $\sim 77,550$ km.

the bending wave that harbors it, form the subject of the present paper.

The Titan nodal bending wave is located ~ 300 km interior to the 170 km-wide Colombo gap, which is home to an narrow, opaque and eccentric ring generally known as the Titan ringlet. The latter is so-named because of its close association with the Titan apsidal resonance, where the local apsidal precession rate of ring particles matches the mean motion of Titan.¹ An overall view of the inner C ring, and of the region including the Colombo gap, the Titan ringlet and the nodal bending wave is provided in Fig. 1. Studies of the Titan ringlet by Porco et al. (1984) demonstrated that it is well-described by a simple keplerian ellipse, precessing under the influence of Saturn's zonal gravity harmonics. But because it is located very near the Titan 1:0 ILR, and because its apoapse is closely aligned with Titan, Porco et al. (1984) concluded that the ringlet's eccentricity is likely to be forced by the apsidal resonance. This idea was further pursued by Nicholson and Porco (1988), who used the ringlet's eccentricity to place a constraint on Saturn's zonal gravity harmonics. A recent reanalysis of the Titan ringlet by Nicholson et al. (2014b) using *Cassini* data confirmed this picture and provided improved orbital elements for the ringlet, while also identifying similar but smaller-amplitude forced eccentricities for many other sharp-edged features in this region of the C ring. We shall see below that these radial distortions also extend across the bending wave.

We begin with a review of the relevant characteristics of vertical resonances and bending waves in Section 2, before providing

a brief description of our occultation dataset in Section 3. In Section 4 we discuss our measurements, orbital fits and the underlying kinematic model. We summarize our conclusions and discuss the possible origin of the bending wave gap in Section 5.

2. Theoretical background

2.1. Resonance geometries

Our kinematic model for the Titan bending wave gap is based on a simple consideration of the geometry associated with Lindblad and vertical resonances, and in particular with apsidal and nodal resonances. In this section we review the basic resonance equations, including the pattern speeds and orbit geometries relevant to our problem. For a more general discussion of resonant perturbations in rings, the interested reader is referred to Appendix A of Nicholson et al. (2014b) or to the text by Murray and Dermott (1999).

Vertical resonances have much in common with the more familiar Lindblad, or eccentric, resonances. In the vicinity of a Lindblad resonance, a ring particle experiences radial force variations due to a particular component of the satellite's gravitational potential at a frequency equal to its natural radial oscillation, or epicyclic frequency κ . The situation is similar at a vertical resonance, where the ring particle experiences out-of-plane force variations at a frequency equal to its natural vertical oscillation frequency μ . For a potential component that varies with longitude and time as $e^{i(m\lambda - \omega t)}$, the resonant condition is

$$m(n - \Omega_p) = \pm \mu. \quad (1)$$

¹ This resonance is a special case of an inner Lindblad resonance (ILR), and is often referred to as the 1:0 ILR.

where m is an integer, n is the ring particle's keplerian angular velocity and the *pattern speed* of the potential is defined by its angular rotation rate $\Omega_p = \omega/m$. In this expression, the + sign corresponds to an inner vertical resonance (IVR), where $n > \Omega_p$, and the - sign corresponds to an outer vertical resonance (OVR), where $n < \Omega_p$. Since $\mu = n - \dot{\Omega}_{\text{sec}}$, where $\dot{\Omega}_{\text{sec}}$ is the local nodal regression rate, we have the equivalent expression for an IVR of

$$m\Omega_p = (m - 1)n + \dot{\Omega}_{\text{sec}}. \quad (2)$$

Vertical resonances only arise when the perturbing moon is on an inclined orbit, and the pattern speed thus depends partly on the satellite's own vertical frequency $\mu' = n' - \dot{\Omega}'_{\text{sec}}$ as well as its orbital mean motion n' . In general, the frequencies of such perturbations can be written as

$$\omega \equiv m\Omega_p = mn' + k\kappa' + p\mu' \quad (3)$$

where $\kappa' = n' - \dot{\varpi}'_{\text{sec}}$ is the satellite's epicyclic frequency and k and p are integers. For the Titan nodal (or -1:0) resonance, we have $m = 1$ and $k = p = -1$, so that we have the resonant condition

$$\dot{\varpi}_{\text{sec}} = \Omega_p = n' - \kappa' - \mu' = -n' + \dot{\varpi}'_{\text{sec}} + \dot{\Omega}'_{\text{sec}}. \quad (4)$$

Here, primed quantities refer to Titan and unprimed quantities to the ring particle. Note that Eq. (4) implies that the pattern speed associated with the nodal resonance is *negative*, but approximately equal in magnitude to Titan's mean motion n_T .

Analogous expressions describe inner and outer Lindblad resonances, with $\mu \rightarrow \kappa$. But in this case, the strongest resonances arise with a satellite on a circular, equatorial orbit and the pattern speed of the perturbation is simply equal to the satellite's keplerian angular velocity, *i.e.*, $\Omega_p = n'$. Such perturbations lead to first-order Lindblad resonances, where

$$m\Omega_p = (m - 1)n + \dot{\varpi}_{\text{sec}} = mn'. \quad (5)$$

An example of such a resonance is the aforementioned Titan apsidal (or 1:0) resonance, where $m = 1$ and the resonance condition becomes simply

$$\dot{\varpi}_{\text{sec}} = \Omega_p = n'. \quad (6)$$

Here $\dot{\varpi}_{\text{sec}} = n - \kappa$ is the local apsidal precession rate and $n' = n_T = 22.577^\circ \text{ d}^{-1}$.

At either the apsidal or nodal resonance, the response of a ring particle is best described in terms of the slowly-changing resonance variable ϕ . For the apsidal resonance this is given by

$$\phi_L = \varpi - \lambda', \quad (7)$$

while for the nodal resonance it is

$$\phi_V = \Omega + \lambda' - \varpi' - \Omega', \quad (8)$$

where λ' is the satellite's mean longitude. For ring particles located exactly at either resonance, we see from Eqs. (6) and (4) that $d\phi_L/dt = 0$ or $d\phi_V/dt = 0$. Examination of the Lagrange perturbation equations shows that stable equilibrium configurations exist only for $\phi = 0$ (when $a < a_{\text{res}}$) or $\phi = \pi$ (when $a > a_{\text{res}}$) (Murray and Dermott, 1999).

An ensemble of ring particles located at or near the apsidal resonance will move on eccentric keplerian orbits given approximately by the expression:

$$r(\lambda, t) \simeq a[1 - e \cos(\lambda - \varpi)]. \quad (9)$$

Substituting for ϖ in terms of ϕ_L , this becomes

$$r(\lambda, t) \simeq a[1 - e \cos(\lambda - \lambda_T - \phi_L)]. \quad (10)$$

where we have used the more specific 'T' subscript to denote Titan's orbital elements. In physical terms, this means that the orbits of the perturbed ring particles form a set of nested ellipses that

revolve around the planet at the same rate as Titan's orbital motion. Either the pericenter or apocenter of the ellipses are aligned with Titan, depending on the value of ϕ_L .

Indeed, the narrow, opaque ringlet located within the Colombo gap (see Fig. 1) has a semimajor axis that is only ~ 21 km exterior to the Titan apsidal resonance and is quite well-described by this expression (Porco et al., 1984). The current best-fitting model for this ringlet has a radial amplitude for its centerline of $a_e = 22.3 \pm 0.2$ km and a phase, $\phi_L = 173.1 \pm 0.3^\circ$ (Nicholson et al., 2014b), close to the expected value of 180° for orbits exterior to the resonance.

At the nodal resonance, we start with the analogous expression for particles moving on low-inclination keplerian orbits:

$$z(\lambda, t) \simeq a \sin i \sin(\lambda - \Omega). \quad (11)$$

Substituting for Ω in terms of ϕ_V , we obtain

$$z(\lambda, t) \simeq a \sin i \sin(\lambda + \lambda_T - \varpi_T - \Omega_T - \phi_V), \quad (12)$$

where we have again used the more specific 'T' subscript to denote Titan's orbital elements. This expression, along with Eq. (10), forms the basis of our kinematic models in Section 4.

Note that the vertical displacement depends on the angle $\lambda + \lambda_T$, rather than on the difference, as in Eq. (10). In physical terms, this means that the orbits of the perturbed ring particles form a set of nested inclined circles that revolve around the planet at approximately the same rate as Titan's orbital motion, but in the *opposite* direction. (Titan's apse and node, ϖ_T and Ω_T , precess with periods of order 700 yr and may be treated as constants for all practical purposes.) This curious situation arises because inclined orbits regress under the influence of an oblate planet, and because the nodal resonance is third-order, unlike the first-order apsidal resonance.

We conclude this subsection by estimating the locations of the resonant radii for the Titan 1:0 and -1:0 resonances. For this we need accurate values for the local precession rates $\dot{\varpi}_{\text{sec}}$ and $\dot{\Omega}_{\text{sec}}$. We use the same expressions provided by Nicholson and Porco (1988) in their study of the Titan ringlet, which include the effects of Saturn's zonal gravity harmonics J_2 through J_{12} , as well as the secular precession induced by the planet's major satellites, but neglect terms of order $e^2 J_2$. (The latter approximation is sufficient, given that the eccentricities involved here are of order 3×10^{-4} or less.) In fact, the satellite contributions to the precession rates are also negligible: they are of order $1.4 \times 10^{-4} \text{ deg d}^{-1}$ at the distance of the Titan ringlet (Nicholson and Porco, 1988), or $\sim 10^{-5}$ of the dominant J_2 term. Solar and general-relativistic perturbations are even smaller and may be neglected for our purposes.

Using the gravity harmonics of Jacobson (2008), we calculate the predicted radius of the 1:0 ILR to be 77,857.4 km, while the corresponding radius for the -1:0 IVR is 77,521.4 km, or 336 km interior to the ILR. (Although the values of J_8 , J_{10} and J_{12} for Saturn are unknown, we used the same nominal values of -10, 1 and -0.5 adopted by Nicholson and Porco (1988), all in units of 10^{-6} and based on interior models.) In their study of the Titan ringlet, Nicholson et al. (2014b) revised the apsidal resonance location to $a_{\text{res}} = 77,861.5 \pm 0.5$ km by using the observed eccentricity of the ringlet (assumed to be resonantly forced) to estimate its distance from the resonance. On the plausible assumption that this correction of 4.1 km reflects small errors in Saturn's gravity harmonics, especially for J_6 and above, we can similarly adjust the predicted value for the IVR to $a_{\text{res}} = 77,525.5 \pm 0.5$ km.²

² We note that Rosen and Lissauer (1988) followed a similar procedure, but adopted a smaller value of a_{res} for the -1:0 IVR of 77,515 km, based on the estimate for the radius of the Titan 1:0 resonance of $77,852 \pm 13$ km by Nicholson and Porco (1988).

2.2. The nodal bending wave

While we do not attempt to model the bending wave itself in the present work, it is likely that the wave is ultimately responsible for the existence of the gap we are studying. It thus seems wise to recap some of the salient characteristics of bending waves before we embark on our analysis of the occultation data.

In the same manner that Lindblad resonances in Saturn's rings launch spiral density waves that propagate away from the resonant radius, vertical resonances can launch spiral vertical perturbations known as bending waves. For a full theoretical discussion, the interested reader is referred to the review by Shu (1984) and for detailed modeling of bending waves see the papers by Gresh et al. (1986) and Lissauer (1985). Unlike density waves, which propagate outwards from an ILR and inwards from an OLR, bending waves generally propagate inwards from an IVR and outwards from an OVR. This is a consequence of the fact that $\mu > n > \kappa$ in a keplarian disk.

Nodal bending waves, however, violate the usual rule by propagating *outwards* from the IVR that drives them. This is ultimately due to their negative pattern speed (cf. Eq. (4)). They can thus resemble density waves, and in fact have sometimes been mistaken for them (Cuzzi et al., 1981; Tiscareno et al., 2013).

A second aspect of bending waves that sets them apart from density waves is their fundamental geometry. A density wave produces periodic variations in the rings' surface mass density, usually manifested observationally as variations in optical depth or brightness. Bending waves, on the other hand, involve wavelike vertical displacements in the ring plane, without significant variations in surface density. The visibility of such variations depends strongly on the viewing geometry, both on the elevation angle and on the azimuthal direction at which the light ray penetrates the ring plane. Bending waves can even 'disappear' under conditions of near normal viewing or illumination, or when they are observed in a direction parallel to the wave crests. Conversely, they are most visible when observed at low elevation angles, or orthogonal to the wave crests. The unusually low elevation angle of the Voyager radio occultation experiment ($B = 5.6^\circ$) led to a very strong signature for the Mimas 5:3 bending wave in the A ring (Gresh et al., 1986), as well as to the discovery of the Titan 1:0 wave by Rosen and Lissauer (1988). Detailed models for both of these waves led to the conclusion that the radio beam had penetrated the ring plane more than once in the strongest parts of the wave trains, leading to highly non-sinusoidal wave profiles.

The radial wavenumber of a bending wave, like that of a density wave, depends primarily on the surface mass density of the ring, as well as the value of m . At distances of at least a few wavelengths from a_{res} , it is given by the asymptotic expression (Hedman and Nicholson, 2013; Shu, 1984):

$$k(r) = \left[3(m-1) + \frac{21}{2} J_2 \left(\frac{R}{a_{\text{res}}} \right)^2 \right] \frac{M(r-a_{\text{res}})}{2\pi\sigma_0 a_{\text{res}}^4} \quad (13)$$

where σ_0 is the average background surface mass density. Here, M and R are the mass and equatorial radius of the planet. Typical density waves in the C ring have wavelengths of 1–2 km at distances of a few kilometers from a_{res} , corresponding to surface densities of a few g cm^{-2} (Baillié et al., 2011; Hedman and Nicholson, 2014), but for waves driven at nodal resonances, where $m = 1$ and the term proportional to J_2 dominates the quantity in brackets, the wavelengths are much longer.³ As a result, the Titan nodal bending wave has a wavelength of ~ 5 km even at a distance of

25 km from the resonance and its signature can be resolved out to ~ 75 km from a_{res} .

Rosen and Lissauer (1988) provide convenient numerical expressions for the radial wavelength and vertical amplitude of the Titan 1:0 bending wave, in terms of the unknown value of σ_0 :

$$2\pi/k \simeq 209 \frac{\sigma_0}{r - a_{\text{res}}} \text{ km}, \quad (14)$$

and

$$A_V \simeq \frac{334}{\sigma_0^{1/2}} \text{ meters}. \quad (15)$$

These are based on analytic expressions for linear waves derived by Shu (1984).

For the Titan nodal bending wave, we thus expect to see a vertical distortion with an $m = 1$ spiral pattern, rotating opposite to the direction of orbital motion with a pattern speed $\Omega_p \simeq -n_T = -22.577^\circ \text{ d}^{-1}$, and propagating outwards from the IVR at ~ 77 , 525 km. A final quirk is that this wave is expected to take the form of a leading spiral, unlike the more common trailing waves with $m \neq 1$. This is yet another consequence of the negative pattern speed.

3. Observations

For the present study, we use data from a series of 44 stellar occultations observed by the Visual and Infrared Mapping Spectrometer (VIMS) on the Cassini spacecraft (Brown et al., 2004). In occultation mode, the instrument's imaging capability is disabled and it stares in a fixed direction towards the target star. At every integration (typically 20–80 ms in duration), a 31-channel spectrum of the star is acquired and recorded, along with the start time of the measurement. In order to reduce background light from the rings to a minimum, we use only the data obtained at a wavelength of 2.9 microns, corresponding to a very strong water ice absorption band. The measured stellar flux as a function of time is converted to the line-of-sight transmission through the rings T , by normalizing the observed count rate by that obtained when the star is seen outside the rings, and then to normal optical depth via the usual expression

$$\tau_n = -\sin |B_*| \ln(T) \quad (16)$$

where B_* is the elevation of the star above the ring plane. The response of the instrument to the incident flux is quite linear, to within the accuracy of ground calibrations, but the signal to noise ratio varies considerably between datasets, primarily because of the varying brightness of the stars employed. Typically, the instrumental noise level is $< 1\%$ and the statistical errors in τ_n are < 0.01 . However, the zero level for τ_n can vary during the course of an occultation if the star moves slightly within the field of view of the detector, changing the unocculted stellar count rate; we do not attempt to correct such systematic errors here as we are primarily interested in the locations of features rather than in modeling their optical depths. For further details on how these observations are made and reduced the reader is referred to the papers by Hedman et al. (2007b); Nicholson and Hedman (2010) or Hedman and Nicholson (2013).

Occultation geometry is calculated based on the reconstructed spacecraft trajectory, the known position of the star from the Hipparcos catalog, corrected for proper motion and parallax at Saturn (ESA, 1997) and the direction of Saturn's pole (Jacobson et al., 2011). Such *ab initio* calculations, however, are typically in error by ~ 1 km, due mostly to residual trajectory uncertainties, so we also apply a simple timing correction to each dataset based on an analysis by R.G. French of a large suite of occultations by circular ring features. (See Nicholson et al., 2014a for more details.) The resulting ring radii are on a scale that is internally consistent to

³ This arises due to the absence of the particle's mean motion in the resonance conditions, Eqs. (6) and (4).

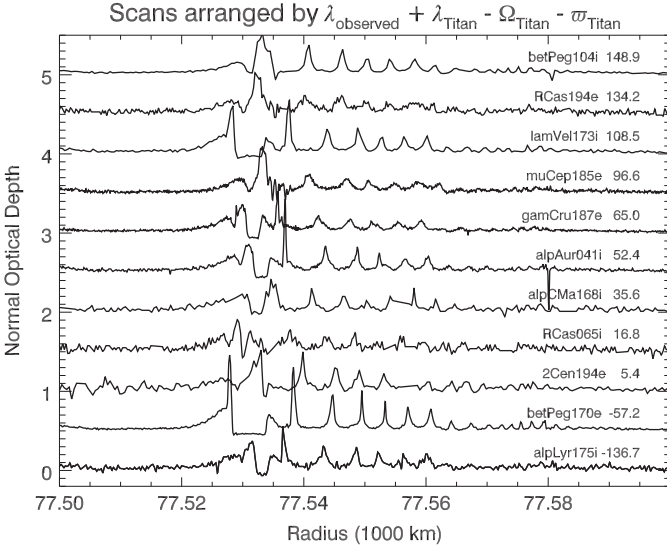


Fig. 2. The region of the Titan –1:0 bending wave as seen in a series of optical depth profiles derived from VIMS stellar occultations obtained over a period of 6 years, for a wide range of geometries. The individual profiles are offset vertically and arranged in order of increasing phase parameter $\theta = \lambda + \lambda_T - \varpi_T - \Omega_T$, as labeled on each profile. The Titan –1:0 IVR is located at a radius of 77,525 km (see text). In most profiles between 5 and 7 wave crests can be seen. Note the variable-width gap that appears at ~ 77.532 km in many of the profiles.

within 200 m, and whose *absolute* uncertainty is believed to be ~ 300 m or less. The final product for each occultation is thus a radial profile of normal optical depth $\tau_n(r)$ at an effective wavelength of $2.9\text{ }\mu\text{m}$.

In Fig. 2 we present a series of profiles for the region containing the Titan nodal bending wave, obtained from 11 occultations observed between March 2007 and July 2013. Each profile is identified by the name of the star and by a number (the ‘Rev’) that identifies the particular Cassini orbit on which the observation was obtained; an appended ‘i’ or ‘e’ indicates the ingress or egress portion of the occultation, some of which yielded two cuts across the C ring. These particular profiles were chosen for their high signal to noise ratios, and also to illustrate the variable appearance of the wave and of the embedded narrow gap. The profiles are arranged in order of increasing values of the vertical phase parameter

$$\theta = \lambda + \lambda_T - \varpi_T - \Omega_T, \quad (17)$$

following Eq. (12). In the best data, as many as twelve crests can be identified in the wave between radii of 77,535 and 77,575 km, but in all cases the amplitude of the wave seems to decrease noticeably and abruptly at $\sim 77,560$ km. A similar decrease was observed in the Voyager occultation data by Rosen and Lissauer (1988), who refer to the strong-wave region as the ‘near wave’ and the weak-wave region as the ‘far wave’. We will also adopt this convenient terminology. In some data sets – most notably the two β Peg occultations shown here – the wave profile is strongly peaked, suggesting that the line of sight to the star is almost tangential to the distorted ring plane at these locations. These generally correspond to stars with smaller elevation angles with respect to the ring plane; for β Peg, $B_* = 31.7^\circ$.

Turning now to the gap seen in the inner part of many of these wave profiles at a radius of $\sim 77,532$ km, we see a surprising diversity in its appearance, although in no case do we see a gap as wide as the 15 km observed in the Voyager RSS occultation profile (Rosen and Lissauer, 1988). Instead, the gap is widest in the β Peg 170 and λ Vel 173 profiles, where its radial width is 5.6 and 4.6 km, respectively. It is narrowest in R Cas 65 at ~ 0.8 km. In several of the profiles shown in Fig. 2, there is no gap at all, but

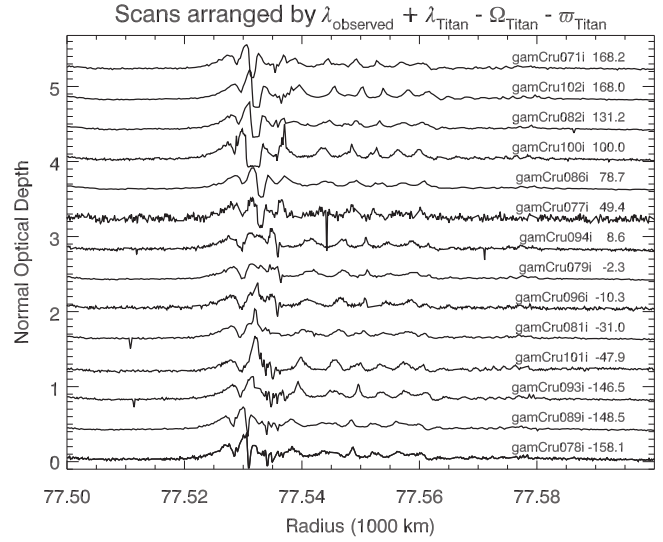


Fig. 3. The region of the Titan –1:0 bending wave as seen in a series of 14 optical depth profiles derived from VIMS γ Cru occultations with very similar geometry. The individual profiles are offset vertically and arranged in order of increasing phase parameter $\theta = \lambda + \lambda_T - \varpi_T - \Omega_T$, as labeled on each profile. The Titan –1:0 IVR is located at a radius of 77,525 km. Note the gradual change in appearance of the region at 77,532 km from a gap to a peak at $\theta \sim -147^\circ$, and then back to a gap at $\theta \sim +49^\circ$. Also visible here is the outward progression of the bending wave crests with increasing phase, indicative of a leading spiral waveform.

rather a local peak in optical depth at about the same radius. This peak ranges in width from ~ 1.2 km in R Cas 194 and μ Cep 185 to 3.0 km for β Peg 104. When we do see a gap, frequently it is flanked by maxima in optical depth. Conversely, when we see a peak there is often a very narrow dip on one or both sides, though not an empty gap; the two β Peg profiles provide perhaps the best examples.

On first inspection, the variable appearance of the gap in Fig. 2 appears to be random, both in time and with respect to the phase parameter θ that is expected to control vertical perturbations by the nearby Titan –1:0 IVR (cf. Eq. 12). But if this variable appearance is due in part to vertical distortions, then we also need to consider the effect of the varying observation geometry between the occultations.

Fortunately a convenient way to control for viewing geometry is provided by a sequence of 17 occultations of the star γ Cru observed over an 8-month period in 2008/2009. All of these occultations have very similar geometry, with identical stellar elevation angles, $B_* = -62.35^\circ$ and inertial longitudes that lie within a fairly limited range ($\sim 50^\circ$). In Fig. 3 we present profiles from 14 of these occultations, again sorted by the phase parameter θ . A much clearer pattern now emerges in the region around the gap at 77,532 km.

Starting at the bottom of this figure, at $\theta \simeq -150^\circ$, we see two profiles with extremely narrow gaps (~ 0.5 km). The next three profiles, from Revs 93, 101 and 81, span a fairly wide range of $-147^\circ < \theta < -31^\circ$ and all show prominent but narrow peaks, of which the widest is γ Cru 101 at -47.9° . Above these we have three profiles that might be described as ambiguous, from Revs 96, 79 and 94, all of which fall in a restricted range of phase between -10.3° and $+8.6^\circ$. But starting at Rev 77 at $\theta = +49.4^\circ$, and continuing through Rev 71 at $+168.2^\circ$, all six remaining profiles show definite gaps. Moreover, these gaps vary systematically in width, reaching a maximum of 2.4 km at $\theta = 100^\circ$ for γ Cru 100.

This systematic variation in gap/peak morphology is evidently strongly correlated with the phase parameter θ , which in turn suggests that the underlying cause is to be found in vertical

distortions of the ring plane by the Titan –1:0 resonance. To a first approximation, we see a periodic variation in peak or gap width with extrema at $\theta \sim -50^\circ$ and $\sim +100^\circ$ and transitions between peak and gap morphology at $\theta \sim -147^\circ$ and $\sim +10^\circ$. That this correlation with θ is not simply a coincidence is demonstrated by the fact that, over the 8-month time span of the γ Cru occultations, the pattern of vertical distortions due to the Titan IVR has rotated by $\sim 8 \times 30 \times 22.5^\circ \text{ d}^{-1} \simeq 5400^\circ$, or 15 complete revolutions around the planet. The probability that we should see such a correlation by chance is thus very small indeed. We therefore conclude that the apparent variations in the radial width of the gap at $\sim 77,532$ km are in all probability revolving around Saturn at a pattern speed of $\Omega_p \simeq -n_T$, as expected for perturbations forced by the Titan –1:0 IVR. In the next section we develop a simple geometric model that can account quantitatively for these variations, not only in the γ Cru data but in all of the available VIMS occultation profiles.

[Fig. 3](#) also serves to illuminate the geometry of the bending wave itself. Note that the wave appears relatively muted in these profiles, due to the high elevation angle. If one mentally connects the peaks in (apparent) optical depth from one profile to the next it is also clear that the radius of any given peak increases with increasing values of θ , or equivalently with increasing inertial longitude at a given instant of time. This implies that the wave is indeed a *leading spiral*, as predicted by [Rosen and Lissauer \(1988\)](#). This sets it apart from all other known density and bending waves seen in Saturn's rings with the exception of the Iapetus –1:0 wave ([Tiscareno et al., 2013](#)). Furthermore, it is apparent on closer inspection of this figure that there is only a single arm in the spiral, as tracing any peak from bottom to top of the diagram brings one to the next peak in the wave. The $m = 1$ nature of the nodal bending wave is thus also confirmed by our observations. Note that in most of the γ Cru profiles only the near-wave region is clearly visible, at $r < 77,560$ km, unlike the situation for the lower-elevation occultations in [Fig. 2](#) where the wave can be traced as far as $\sim 77,585$ km in some instances.

Before leaving [Fig. 3](#), we draw the reader's attention to two narrow features located on either side of the prominent gap at 77,532 km. In particular, there is a persistent minimum in optical depth at $\sim 77,528$ km, while at $\sim 77,535$ km there is a narrow feature that often appears as a gap, but in a few instances, such as the γ Cru profiles for revs 77 and 100, appears instead as a peak in optical depth. These features are also seen in several of the profiles in [Fig. 2](#). They do not appear to form part of the bending wave itself and we will return to their possible interpretation in [Section 5](#).

4. Data analysis

4.1. Modeling the gap width variations

The variations in gap width seen in [Fig. 3](#), where the occultation geometry is quite similar for each observation, strongly suggest that the underlying perturbation is vertical in nature, and forced by the Titan –1:0 nodal resonance. A simple model that could account for these observations involves a narrow gap of uniform width, either or both of whose edges is perturbed vertically by the IVR. A sketch of such a model is presented in [Fig. 9](#) below. As the pattern of perturbations rotates at the pattern speed $\Omega_p \simeq -n_T$, the inner and outer edges will alternately approach and recede from one another, when viewed from any direction other than at normal incidence. If the vertical amplitude of the inclined edge(s) is sufficiently large, then the two edges will appear to overlap at some phases and the gap will disappear. A minimum requirement for this to happen is that the vertical amplitude A_V be greater than $\Delta r \tan B_*$, where Δr is the radial gap width and B_* is the elevation of the stellar line of sight with respect to the ring plane. To first or-

der, it does not matter whether it is the inner or outer edge that is perturbed, or if both edges are perturbed with differing amplitudes and/or phases; only the differences in amplitude and/or phase between the two edges are really important to the gap width variations.

In order to test such a model, we first need to quantify the variations in gap width seen in [Figs. 2](#) and [3](#). To this end, we wrote an automated procedure that first searches for an empty gap within the radial range 77,528.0 to 77,535.0 km⁴ in each occultation profile, and then determines the radii within this range of the falling and rising edges. These are defined as the points where the gradient $d\tau/dr$ is negative and the largest in magnitude (r_1) or positive and largest in magnitude (r_2). In the event that no gap is found, then the program searches for a peak, defined by the criterion that the maximum optical depth exceeds 0.35.⁵ Again, the falling and rising edges are measured and designated r_1 and r_2 . In each case, the apparent radial width of the gap W is recorded as $r_2 - r_1$, but a negative value of W indicates a peak in τ instead of a gap. All measured profiles were inspected by eye to verify that the edges identified by the automated procedure were sensible. Uncertainties in r_1 and r_2 are estimated by taking the difference in radius between adjacent samples in each data set, as we did not attempt to interpolate between points. These do not include systematic uncertainties in the radius scale for each occultation, though as noted above these are believed to be only ~ 200 m. For the Voyager RSS occultation, we assumed uncertainties in r_1 and r_2 of 400 m, the radial resolution of the diffraction-corrected profile.

[Table 1](#) lists our measured radii, r_1 and r_2 , along with the corresponding event time measured in seconds from the J2000 epoch (2000 Jan 1.5 ET), ring longitude λ , the value of B_* , Titan's angular elements λ_T , Ω_T and ϖ_T , the phase parameter θ and several other secondary quantities defined below. In [Fig. 4](#) we show selected profiles with the corresponding measured edge radii, chosen to illustrate both wide and narrow gaps as well as peaks of varying width. Optical depth profiles of the gap region for all of our measured occultation profiles are shown at higher resolution in Appendix A. Out of a total of 44 occultation profiles, 29 yielded useful measurements, seven of which are peaks and the remainder are gaps. Measured widths vary from -3.0 to 5.6 km. In ten cases where no clear gap or peak was identified, or where the visible gap was too narrow to measure accurately, the radii in the table are set to zero. An additional five profiles were discarded because of an unfortunately-located data dropout.⁶ [Table 2](#) provides a list of the 15 occultation profiles that were not included in our analysis, together with a brief explanation of the reason(s) for omitting each one, and whether or not an obvious gap or peak is seen in the data.

Our first model assumes a constant intrinsic radial gap width W_0 , and vertical distortions at one or both edges for which the differential amplitude is governed by [Eq. \(12\)](#):

$$\Delta z(\lambda, t) = A_G \sin(\theta - \phi_V), \quad (18)$$

where we again use the shorthand notation $\theta = \lambda + \lambda_T - \varpi_T - \Omega_T$. The parameter A_G is the difference in vertical amplitude, $a \sin \Delta i$ between the outer and inner edges of the gap. (For simplicity, we have assumed here that the ascending nodes of both edges are aligned, *i.e.*, that the resonance variable ϕ_V is the same at both edges. We will relax this assumption in the next section.) The apparent radial offset of a ring segment in an occultation profile

⁴ Except for the Voyager RSS occultation, where the radial range was 77,510–77,540 km

⁵ Except for the Rev 104 β Pegasus occultation, where a maximum optical depth of 0.1 was used.

⁶ The VIMS instrument pauses briefly after every 64 samples to obtain an instrumental background measurement, resulting in periodic gaps in the light curve.

Table 1

Occultation observations of the gap in the Titan –1:0 bending wave.

Star	Rev	ET (seconds)	r_1 (km)	r_2 (km)	λ_R	B_*	λ_*	λ_T	Ω_T	ϖ_T	$\lambda_R - \lambda_T$	θ	$\lambda_R - \lambda_*$	β	
alpAur	034	i	218339789.285	77532.570 ± 0.886	77533.453 ± 0.887	17.5	50.9	-46.6	179.9	-110.9	-152.4	-162.4	100.7	64.2	0.354
RHya	036	i	220948858.922	0.000 ± 0.000	0.000 ± 0.000	170.3	-29.4	70.8	140.2	-110.8	-152.4	30.2	-146.3	99.5	0.293
alpAur	041	i	227949821.298	77531.719 ± 0.157	77534.078 ± 0.157	338.8	50.9	-46.6	170.6	-110.8	-152.2	168.2	52.4	25.4	0.734
RCas	065	i	262013534.368	77529.688 ± 0.273	77530.508 ± 0.273	43.1	56.0	-137.1	71.4	-110.7	-151.6	-28.3	16.8	-179.8	-0.673
gamCru	071	i	266193909.739	77530.922 ± 0.281	77532.055 ± 0.283	182.6	-62.3	50.7	83.3	-110.7	-151.6	99.3	168.2	131.9	0.350
gamCru	073	i	267426581.797	0.000 ± 0.000	0.000 ± 0.000	181.6	-62.3	50.7	47.1	-110.7	-151.5	134.5	130.9	130.9	0.343
gamCru	077	i	269858704.956	77532.469 ± 0.144	77533.477 ± 0.143	180.5	-62.3	50.7	-33.4	-110.8	-151.5	-146.1	49.4	129.8	0.336
gamCru	078	i	270467180.572	77530.758 ± 0.144	77531.188 ± 0.144	180.3	-62.3	50.7	119.4	-110.8	-151.5	60.9	-158.1	129.6	0.334
gamCru	079	i	271046046.578	0.000 ± 0.000	0.000 ± 0.000	178.5	-62.3	50.7	-83.0	-110.8	-151.4	-98.5	-2.3	127.8	0.321
gamCru	081	i	272320912.482	77532.477 ± 0.267	77531.672 ± 0.267	177.6	-62.3	50.7	-110.8	-110.8	-151.4	-71.6	-31.0	127.0	0.315
gamCru	082	i	272956697.097	77531.383 ± 0.268	77532.977 ± 0.267	177.2	-62.3	50.7	51.9	-110.8	-151.4	125.3	131.2	126.5	0.312
gamCru	086	i	275504222.525	77532.227 ± 0.400	77533.828 ± 0.400	176.1	-62.3	50.7	0.5	-110.8	-151.4	175.6	78.7	125.4	0.304
gamCru	089	i	277409273.905	77530.531 ± 0.268	77531.070 ± 0.268	175.8	-62.3	50.7	133.5	-110.8	-151.3	42.3	-148.5	125.2	0.302
gamCru	093	i	280045799.684	0.000 ± 0.000	0.000 ± 0.000	208.9	-62.3	50.7	102.5	-110.8	-151.3	106.5	-146.5	158.2	0.487
gamCru	094	i	280681953.353	0.000 ± 0.000	0.000 ± 0.000	191.6	-62.3	50.7	-85.1	-110.8	-151.2	-83.2	8.6	140.9	0.407
gamCru	096	i	282014757.256	0.000 ± 0.000	0.000 ± 0.000	184.9	-62.3	50.7	-97.2	-110.9	-151.2	-77.9	-10.3	134.2	0.365
gamCru	100	i	285034650.489	77530.547 ± 0.142	77532.961 ± 0.142	225.9	-62.3	50.7	-27.9	-110.9	-151.2	-106.2	100.0	175.2	0.522
gamCru	101	i	285861804.302	0.000 ± 0.000	0.000 ± 0.000	225.9	-62.3	50.7	-175.9	-110.9	-151.2	41.8	-47.9	175.2	0.522
gamCru	102	i	286686970.887	77531.391 ± 0.342	77533.102 ± 0.342	225.5	-62.3	50.7	40.4	-110.9	-151.2	-174.8	168.0	174.9	0.522
TXCam	102	i	286988465.218	0.000 ± 0.000	0.000 ± 0.000	302.9	61.3	-48.8	116.5	-110.9	-151.2	-173.6	-38.5	-8.3	0.542
betPeg	104	i	288914760.900	77535.055 ± 0.423	77532.094 ± 0.423	341.0	31.7	-147.7	-94.1	-110.9	-151.1	75.0	148.9	128.7	-1.013
alpAur	112	i	297808816.493	0.000 ± 0.000	0.000 ± 0.000	8.2	50.9	-46.6	65.3	-111.1	-151.0	-57.1	-24.5	54.8	0.468
alpOri	117	i	304633645.446	0.000 ± 0.000	0.000 ± 0.000	44.3	11.7	-41.0	49.5	-111.2	-150.8	-5.2	-4.3	85.3	0.400
omiCet	135	i	333276705.145	0.000 ± 0.000	0.000 ± 0.000	347.5	3.5	-95.7	-22.1	-111.7	-150.3	9.6	-132.7	83.2	1.958
alpCMa	168	i	394197559.388	77530.977 ± 0.391	77533.320 ± 0.390	80.8	-13.5	-30.8	53.1	-112.5	-149.3	27.7	35.6	111.6	1.533
alpCMa	169	i	396265908.655	77532.172 ± 0.389	77531.008 ± 0.389	80.4	-13.5	-30.8	-123.8	-112.5	-149.2	-155.8	-141.7	111.2	1.508
betPeg	170	e	397972561.762	77528.117 ± 0.175	77533.703 ± 0.175	77.2	31.7	-147.7	-36.2	-112.5	-149.2	113.3	-57.2	-135.1	-1.147
betPeg	172	i	401621329.364	0.000 ± 0.000	0.000 ± 0.000	313.7	31.7	-147.7	-166.7	-112.6	-149.2	120.4	48.7	101.4	-0.320
lamVel	173	i	403834486.398	77528.883 ± 0.384	77533.492 ± 0.384	155.4	-43.8	0.3	51.4	-112.6	-149.2	104.0	108.5	155.1	0.946
alpLyr	175	i	406604371.860	77531.953 ± 0.248	77534.188 ± 0.248	266.6	35.2	144.6	55.0	-112.6	-149.1	-148.4	-136.7	122.0	-0.751
WHya	179	i	411903454.213	77532.883 ± 0.144	77532.445 ± 0.144	149.1	-34.6	75.7	2.6	-112.6	-149.0	146.4	53.4	73.3	-0.415
WHya	180	i	413052876.409	77531.242 ± 0.142	77532.945 ± 0.142	149.7	-34.6	75.7	-55.3	-112.6	-149.0	-155.0	-4.0	73.9	-0.400
WHya	181	i	414202115.325	77530.078 ± 0.142	77532.492 ± 0.142	149.8	-34.6	75.7	-116.6	-112.6	-148.9	-93.7	-65.2	74.0	-0.398
muCep	185	e	418014163.987	77533.938 ± 0.087	77532.641 ± 0.087	39.9	59.9	-175.5	155.1	-112.7	-148.9	-115.3	96.6	-144.7	-0.473
RCas	185	i	418068359.832	0.000 ± 0.000	0.000 ± 0.000	334.2	56.0	-137.1	169.9	-112.7	-148.9	164.3	45.6	111.3	-0.244
gamCru	187	i	419920448.053	77532.812 ± 0.099	77533.211 ± 0.099	155.5	-62.4	50.7	-60.8	-112.6	-148.9	-143.7	-3.8	104.8	0.134
gamCru	187	e	419929826.253	77530.602 ± 0.099	77532.492 ± 0.396	221.8	-62.4	50.7	-58.3	-112.6	-148.9	-79.9	65.0	171.1	0.518
muCep	191	i	423057424.470	77531.648 ± 0.195	77532.820 ± 0.195	290.7	59.9	-175.5	35.4	-112.6	-148.9	-104.7	-132.4	106.2	-0.162
RCar	191	i	423391571.838	77529.750 ± 0.229	77530.898 ± 0.229	146.5	-63.5	-0.2	119.7	-112.7	-148.8	26.8	167.7	146.7	0.417
RCas	191	i	423133926.880	0.000 ± 0.000	0.000 ± 0.000	297.7	56.0	-137.1	54.3	-112.6	-148.9	-116.7	-106.5	74.8	0.177
muCep	193	i	425124139.750	0.000 ± 0.000	0.000 ± 0.000	290.9	59.9	-175.5	-144.0	-112.6	-148.8	75.0	48.4	106.4	-0.164
2Cen	194	i	426575188.025	77530.484 ± 0.401	77532.094 ± 0.401	157.6	-40.7	75.6	-123.8	-112.6	-148.8	-78.6	-64.8	82.0	-0.161
2Cen	194	e	426584852.205	77533.438 ± 0.401	77531.430 ± 0.401	225.1	-40.7	75.6	-121.1	-112.6	-148.8	-13.8	5.4	149.5	1.001
RCas	194	e	426259216.449	77532.859 ± 0.229	77531.711 ± 0.229	83.3	56.0	-137.1	149.5	-112.7	-148.8	-66.2	134.2	-139.6	-0.513

Table 2
List of rejected occultation profiles.

Star/rev	θ^a	β^b	Data gap?	Notes
R Hya 036	-146	0.30		Unresolved gap
gamCru 073	131	0.34	Y	1–2 km wide gap
gamCru 079	-2	0.32		No obvious feature
gamCru 093	-146	0.49	Y	No obvious feature
gamCru 094	9	0.41		No obvious feature
gamCru 096	-10	0.36	Y	Narrow peak?
gamCru 101	-48	0.52	Y	1–2 km wide peak
TX Cam 102	-38	0.54		2 km peak; bad geometry
alpAur 112	-24	0.47		2 km peak; low resol'n
alpOri 117	-4	0.40		No obvious feature
omiCet 135	-133	1.96		Broad, indistinct peak; low resol'n
betPeg 172	49	-0.32	Y	No obvious feature
R Cas 185	46	-0.24		Indistinct narrow peak
R Cas 191	-106	0.18		Indistinct narrow peak
muCep 193	48	-0.16		No obvious feature

^a $\theta = \lambda + \lambda_T - \varpi_T - \Omega_T$.^b $\beta = (\tan B_{\text{eff}})^{-1} = \cos(\lambda - \lambda_*) / \tan B_*$.

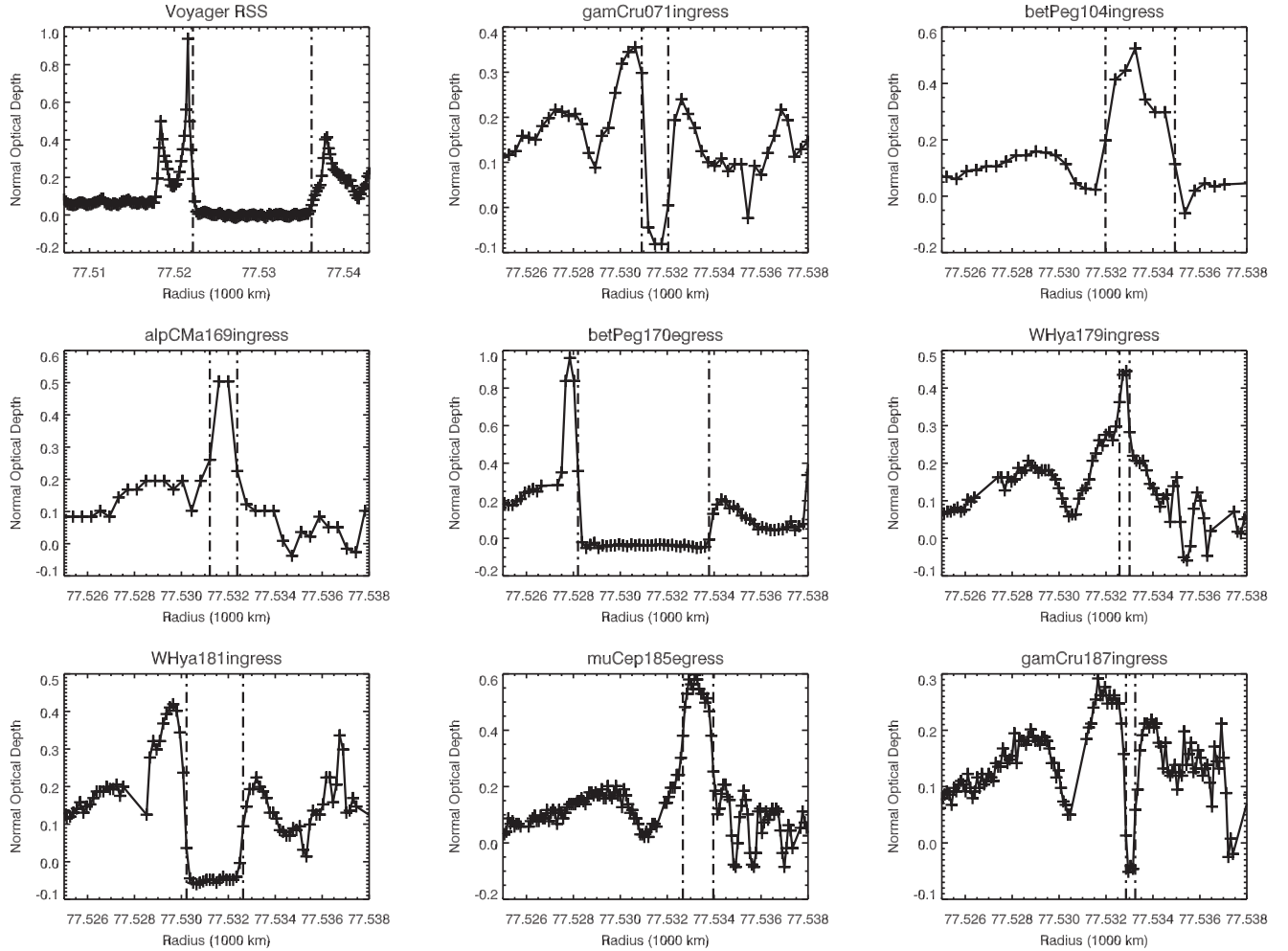


Fig. 4. A subset of occultation profiles for the region of the gap seen in the Titan –1:0 bending wave illustrating our measurements of the inner and outer gap edges. These are indicated by vertical dot-dashed lines. The first profile is from the *Voyager 1* RSS occultation, while the remainder are from *Cassini* VIMS stellar occultations, as labeled. Crosses indicate individual occultation measurements, acquired at intervals of 20 to 80 ms. Short data gaps in some VIMS profiles (e.g., W Hya 179i or W Hya 181i) indicate periods of background measurement. The apparent gap width is greatest in the *Voyager 1* and β Peg 170e profiles, and narrowest in γ Cru 187i. The widest peak is in β Peg 104i and the narrowest is in W Hya 179i.

depends on its vertical displacement z , on B_* , and on the longitude of observation λ . If the inertial longitude of the line of sight to the star, projected onto the ring plane, is denoted by λ_* , then the apparent radial displacement is given by $\delta r = -z/\tan B_{\text{eff}}$, where the effective elevation angle, B_{eff} is given by Gresh et al. (1986); Jerousek et al. (2011); Nicholson et al. (1990):

$$\tan B_{\text{eff}} = \frac{\tan B_*}{\cos(\lambda - \lambda_*)}. \quad (19)$$

For any particular star, both B_* and λ_* are fixed, but we see that δr depends on z and λ , both of which vary between occultations. For occultations near the ring ansae (where $\lambda - \lambda_* \simeq \pm 90^\circ$), $B_{\text{eff}} \rightarrow \pm 90^\circ$ and the radial displacement is almost zero, even if z is substantial. But for occultation cuts near the sub-spacecraft point or its antipode, where $\lambda - \lambda_* \simeq 180^\circ$ or 0° , $B_{\text{eff}} \simeq \pm B_*$. In such a situation, especially if $|B_*|$ is small, the apparent radial displacement z can be much greater than the actual vertical displacement z .

Combining these two expressions, we obtain the following model for the apparent radial width of the gap (or peak):

$$W_{\text{mod}}(\lambda, t) = W_0 - A_G \beta \sin(\theta - \phi_V), \quad (20)$$

where we introduce the convenient parameter $\beta = (\tan B_{\text{eff}})^{-1} = \cos(\lambda - \lambda_*)/\tan B_*$. Note that, in this expression, a negative value of W indicates that the outer edge of the gap will appear at a radius less than that of the inner edge. In such an instance, the two

edges of the gap will overlap along the line of sight to the star, resulting in a doubling of the measured optical depth. This we interpret as the origin of the peaks in the occultation profiles, and the width of the model peak is simply given by $|W|$. Thus our model applies both to gaps and peaks, according as W is positive or negative. We fit this model to the observations using the IDL MPFIT2DFUN routine (Markwardt, 2009), which performs a nonlinear weighted least-squares fit. Individual data points are assigned nominal uncertainties equal to the radial sampling interval of the data set.

Our best fit to the *Cassini* data alone is shown as the red curve in Fig. 5, where we plot both the apparent radial width of the gap $W(\lambda, t)$ vs the phase angle θ in the top panel, and the corresponding inferred vertical displacement $\Delta z = (W_0 - W)/\beta = (W_0 - W) \tan B_{\text{eff}}$ in the bottom panel. Δz is simply the difference between the heights of the outer and inner gap edges at a particular longitude and time. This fit yields a radial gap width, $W_0 = 0.59 \pm 0.07$ km and a vertical amplitude $A_G = 4.35 \pm 0.23$ km. The fitted value of the ascending node corresponds to a resonance variable $\phi_V = 203 \pm 2^\circ$. Note that, with this simple model, we cannot determine if the inner gap edge is less inclined than the outer edge, or vice versa; we only know their differential amplitude. The χ^2 per degree-of-freedom for this fit is 0.56, which suggests that we may have been overly conservative in estimating our

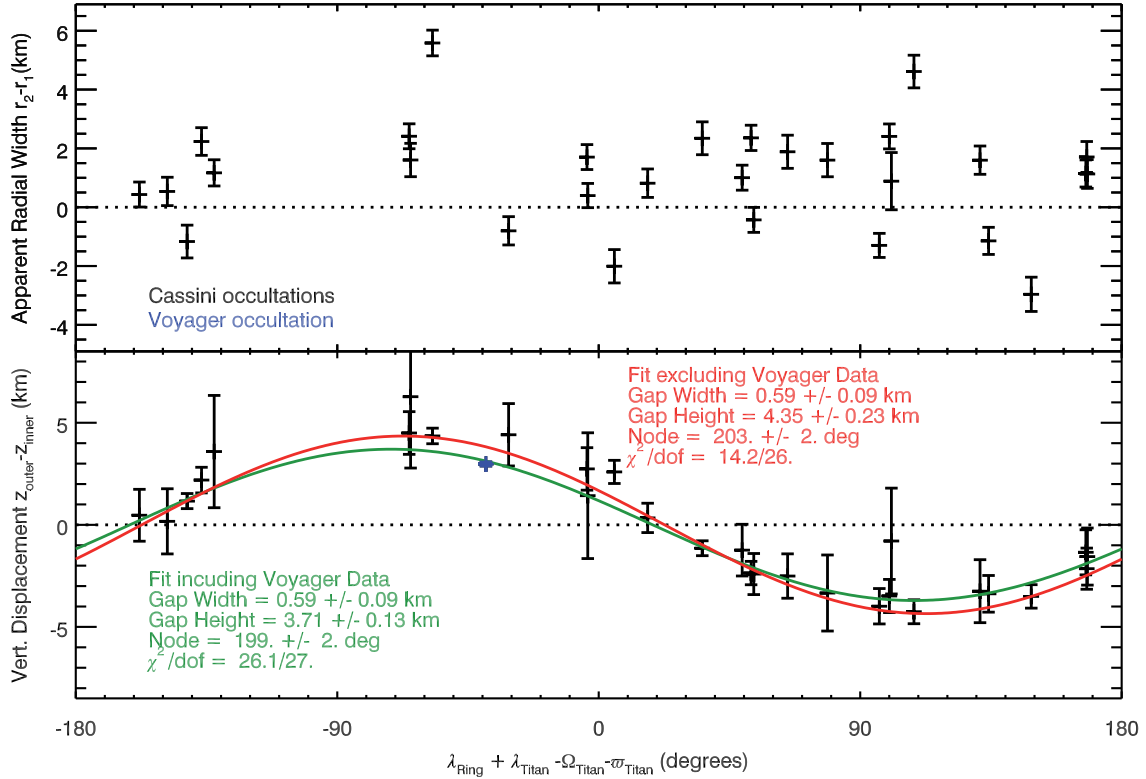


Fig. 5. Apparent radial widths and inferred vertical displacements for the gap at 77,532 km plotted as a function of the phase parameter $\theta = \lambda + \lambda_T - \varpi_T - \Omega_T$. Each occultation is represented by a 'plus' symbol with its corresponding uncertainty. The top panel shows the measured gap widths $W = r_2 - r_1$, where negative values correspond to peaks rather than gaps (see text). The bottom panel shows the inferred vertical displacement Δz between the inner and outer edges of the gap, together with our best-fitting models as described by Eq. (20). The fit shown in red excludes the Voyager RSS point at $\theta = -38.8^\circ$, which is plotted here in blue. The fitted amplitude, $A_G = 4.35 \pm 0.23$ km and the inferred radial width of the gap, $W_0 = 0.59 \pm 0.09$ km. The fit in green includes the Voyager RSS point; it yields a reduced vertical amplitude of 3.71 ± 0.13 km but the same gap width. (Note that the Voyager RSS apparent gap width of 14 km is off-scale in the upper panel.).

measurement uncertainties. The true uncertainties in the fit parameters may thus be smaller than those shown in Fig. 5 by a factor of about $\sqrt{0.56} \simeq 0.75$.

A closer inspection of this figure shows that the gap's vertical amplitude, A_G is primarily constrained by the widest gaps and peaks. The key gaps are β Peg 170, which at $W = 5.6$ km shows the widest gap in the Cassini data, and λ Vel 173 with $W = 4.6$ km. The most important peak is β Peg 104, with $W = 3.0$ km. All of these data points have relatively small uncertainties, and correspond to values of θ near -60° or 120° . (Note that a gap does not necessarily correspond to a positive value of Δz , or vice versa: the two widest gaps (β Peg 170 and λ Vel 173) correspond to $\Delta z = +4.5$ km and -4.3 km, respectively.) The model value of ϕ_V , on the other hand, is best-constrained by data points that fall near the ascending or descending node at $\theta = -160^\circ$ or $+20^\circ$. In our data set this happens to include the two points with the smallest value of B_* : α CMa 168 and 169. These two occultations yielded a relatively narrow gap and peak, with $W = 2.3$ km and -1.2 km, respectively. Should either of these occultation cuts have fallen closer to $\theta = -70^\circ$ or $+110^\circ$, and also well away from the ring ansa, we might have seen a gap as wide as 17 km.

Our Cassini-only model fit in Fig. 5 also comes fairly close to accomodating the Voyager RSS occultation; despite its very large apparent gap width of 14 km, the inferred value of Δz for this datum is within ~ 1 km of the model curve. In this case a very low value of $B_* = 5.6^\circ$, combined with a fortuitous occultation track that crossed the rings well away from the ansa resulted in an unusually large value of $\beta = -4.51$, or $B_{\text{eff}} = -12.5^\circ$. The implied vertical displacement, $\Delta z = -(W - W_0)/\beta = 3.0$ km, whereas the Cassini-

only model predicts that $\Delta z = 3.7$ km. Indeed, when we add the Voyager RSS data point to the fit, as shown by the green curve in Fig. 5, the radial gap width is unchanged at 0.59 ± 0.07 km while the ascending node shifts only slightly to $199 \pm 2^\circ$. However, the vertical amplitude A_G is reduced to 3.71 ± 0.13 km, reflecting the very small error bars on the Voyager measurement and the fact that this datum falls significantly below the Cassini-only model fit.

But the χ^2 per degree-of-freedom for this fit is almost twice that of the Cassini-only fit; requiring the model to fit the Voyager point, whose vertical uncertainty is very small, forces systematic residuals on the Cassini data. This is particularly noticeable in the relatively large residuals for β Peg 170, 2 Cen 194 and β Peg 104, all of which fall at least 1σ outside the green model curve. This suggests that the gap's vertical amplitude may actually have increased somewhat since the Voyager epoch. However, the combined fit is statistically acceptable and suggests that our simple model is largely successful in accounting for both the observed gap width variations in the Cassini data and the anomalously-large width seen in the Voyager RSS profile.

We can gain more insight into why some occultations yield particularly wide gaps, or broad peaks, by plotting the distribution of all the observations vs the two key geometric parameters, θ and $\beta = (\tan B_{\text{eff}})^{-1}$, as shown in Fig. 6. Here, open circles indicate observations with measurable gaps, filled circles indicate observations with clear peaks, and crosses denote ambiguous or otherwise unmeasurable profiles. Dot-dashed lines show contours of constant gap width W , as predicted by the Cassini-only model parameters in Fig. 5, for $W = 1, 2, 3, 4$ and 5 km. Dotted lines show contours of constant peak width for the same absolute values of W . The solid

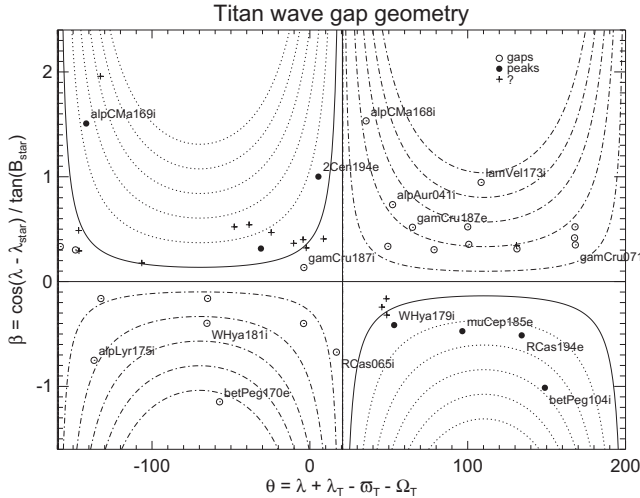


Fig. 6. The distribution of VIMS occultation observations of the Titan nodal bending wave, as a function of the geometric parameters $\theta = \lambda + \lambda_T - \varpi_T - \Omega_T$ and $\beta = \cos(\lambda - \lambda_*)/\tan B_*$. Each occultation is represented by a symbol: open circles denote profiles with gaps at 77,532 km; filled circles denote peaks in optical depth; crosses denote profiles that are ambiguous or could not be measured for any other reason. Dot-dashed lines indicate contours of constant gap width predicted by our Cassini-only model fit, Eq. (20) for $W = 1, 2, 3, 4$ and 5 km, while dotted lines indicate contours of constant peak width for $W = -1, -2, -3, -4$ and -5 km. The solid curve corresponds to an apparent gap width of $W = 0$, where neither a gap nor a peak is expected. Note that most of the ambiguous or unmeasurable profiles lie close to this line. Selected data points are identified, including all profiles shown in Figs. 2 and 4. The band of points with $0.3 < \beta < 0.5$ are almost all γ Cru occs, for which the value of B_{eff} was approximately constant.

lines indicate the critical locus of parameters θ and β for which $W = 0$, i.e., those geometries for which the two gap edges are exactly superimposed along the line of sight to the star. Note that when β is near zero (i.e., when the rings are viewed nearly pole-on, or when the line of sight to the star is near the ring ansa), the gap is seen with its intrinsic width $W = W_0 \simeq 0.6$ km. Likewise, when $\theta \simeq \phi_V$ or $\theta \simeq \phi_V + 180^\circ$, the vertical displacement is small and the gap is again seen with its intrinsic width of ~ 0.6 km. As a result, the diagram can be conveniently divided into four quadrants, with the width $> W_0$ in the first and third quadrants, and $< W_0$ in the second and fourth. Peaks, which appear as negative widths in the data and in our model, should be found only in the latter. Along the boundaries between quadrants, $W = W_0$.

As anticipated, the occultation profiles with the widest gaps all fall in the first and third quadrants, superimposed upon the dot-dashed contours. For example, β Peg 170 falls near the middle of the third quadrant, just beyond the $W = 5$ km contour, while other unusually wide gaps are expected for λ Vel 173 in the first quadrant and W Hya 181 in the third, as observed.⁷ On the other hand, all occultation profiles with definite peaks fall in the second and fourth quadrants, superimposed upon the dotted contours. The most prominent are β Peg 104, μ Cep 185 and R Cas 194, all of which fall in the fourth quadrant. As noted above, these same data are the most important in determining the vertical amplitude of the gap, A_G .

Furthermore, all of the unusually narrow measured gaps (e.g., γ Cru 187i and R Cas 65) as well as all definite narrow peaks (e.g., α CMa 169 and W Hya 179) fall close to the solid lines where $W = 0$, i.e., where the inner and outer edges appear to coincide along the line of sight to the star. We note that most of the unmeasured or ambiguous profiles, denoted by crosses in Fig. 6, also lie close to the solid lines, implying very narrow gaps or peaks.

In a few cases there would appear to be a disagreement between the observations and our simple model, but these can largely be accounted for. The γ Cru 101, TX Cam 102 and α Aur 112 profiles all clearly show a peak, as predicted, but the feature is either too broad to measure or the data are corrupted in some manner, preventing useful measurements. For R Hya 36 the data indeed show an extremely narrow gap, less than 0.5 km wide, but it is only one sample wide and thus not measurable. A very low elevation angle of $B_* = 3.5^\circ$ should have made the α Cet 135 occultation particularly sensitive to vertical distortions, but the star's track passed near the ring ansa, reducing the radial amplification factor β to just 1.96, and the value of $\theta = -132.7^\circ$ is within 25° of the ascending node, where Δz is small. As a result, the model predicts a modest peak of width ~ 3 km, while the data – which are relatively poorly-sampled – show only a very indistinct, broad peak that could not be measured. The α Ori 117 occultation, with our second-lowest elevation angle of $B_* = 11.7^\circ$, also crossed within 5° of the ring ansa, leading to a predicted gap width very near zero. Neither a gap nor a peak is seen in the profile.

We therefore find no case where there is a clear inconsistency between the data and the model predictions.

4.2. Modeling individual gap edges

While the models in Figs. 5 provide a satisfactory fit to the observed variations in the width of the gap near 87,532 km, they leave unresolved the question of which gap edge is inclined. We have also assumed so far that the gap's radial width is constant, which may not be correct, and that the nodes of the inner and outer edges are aligned. We can resolve these issues by fitting the inner and outer gap edges separately, and so determine their individual vertical amplitudes A_V , phases ϕ_V and eccentricities e . A potential downside to such a model is the additional systematic uncertainty introduced by possible errors in the reconstructed radius scale of each occultation, which cancel out when only the gap widths are fitted. A second concern, and the main reason that we did not proceed immediately to such a fit, is the larger number of free parameters it entails. Assigning separate vertical amplitudes and phases to each edge, and allowing for the possibility of nonzero eccentricities, we find that a total of 10 free parameters are needed, vs three for each of the above fits. These are the mean radii a , eccentricities e and pericenters ω for both edges plus values of A_V and ϕ_V for each edge. We can slightly reduce the range of phase space to be studied by assuming that any eccentricities are forced by the nearby Titan 1:0 ILR. This lets us set $\dot{\omega} = n_T$, as has been found for all other noncircular edges in this region (Nicholson et al., 2014b).

Our model for the apparent radius of each edge is specified by a combination of Eqs. (10) and (20):

$$r(\lambda, t) \simeq a[1 - e \cos(\lambda - \lambda_T - \phi_L)] - A_V \beta \sin(\theta - \phi_V), \quad (21)$$

where again the phase parameter $\theta = \lambda + \lambda_T - \varpi_T - \Omega_T$ and the radial amplification factor $\beta = \cos(\lambda - \lambda_*)/\tan B_*$. A_V is the vertical amplitude of the edge in question. The angles ϕ_L and ϕ_V are assumed to be constants for each edge; the former specifies the orientation of the pericenter relative to Titan, and is expected to be near 0 for orbits interior to the Titan 1:0 ILR (Nicholson et al., 2014b). (In principle, either or both of these resonance variables could be librating slowly, or even circulating through 360° , but in the interests of simplicity we will ignore this possibility here. The Titan ringlet seems not to be librating (Nicholson et al., 2014b), but the outer edge of the B ring is known to be circulating with a period of 5.4 yrs (Nicholson et al., 2014a; Spitale and Porco, 2010).)

We fit this model to the edge measurements using the IDL CURVEFIT routine (similar results were obtained with the MPFIT2DFUN routines), with the uncertainty of each data point

⁷ All of the profiles identified in Fig. 6 are shown in Figs. 2 or 4.

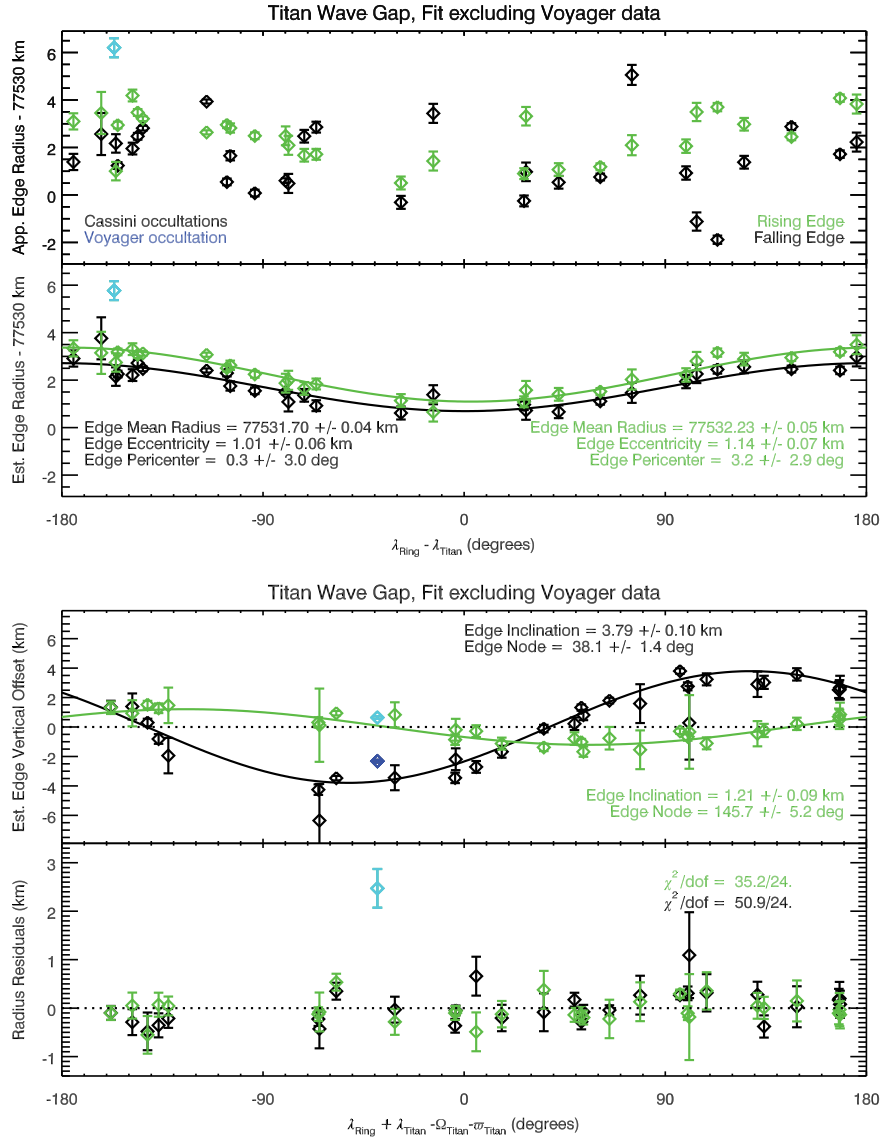


Fig. 7. Apparent radii and inferred radial and vertical displacements for both edges of the gap at 77,532 km. Black points denote the radii of falling edges, r_1 and green denotes rising-edge radii, r_2 . The top panel shows the measured edge radii, as a function of the angle $\lambda - \lambda_T$, while the second panel shows the same radii after removing the contributions due to the fitted vertical displacement of each edge, together with the best-fitting elliptical models. The third panel shows the inferred vertical displacements for both gap edges, after removal of the radial variations due to eccentricity, plotted as a function of the phase parameter $\theta = \lambda + \lambda_T - \omega_T - \Omega_T$, together with our best-fitting vertical models. This fit excludes the Voyager RSS points, which are plotted in blue. The fitted vertical amplitudes are $A_V^{\text{in}} = 3.79 \pm 0.10$ km and 1.21 ± 0.09 km for the inner and outer edges, respectively, while the radial gap width is 0.53 ± 0.07 km. (Note that the Voyager RSS inner gap edge points are off-scale in the first, second and fourth panels.).

again set equal to the sampling interval of the relevant data set. Our best-fitting models are shown in Fig. 7, for the Cassini data alone, and in Fig. 8 with the Voyager RSS data included. Each figure has four panels: the top panel shows the measured radii of the falling and rising gap edges, r_1 and r_2 from Table 1. (Recall here that when $r_2 < r_1$ we have a peak, rather than a gap.) The second panel shows the same radii, after removal of the contributions due to the vertical displacement of the edges, as a function of the angle $\lambda - \lambda_T$; it thus shows only the variations due to eccentricity, along with the appropriate model fits. The third panel shows the inferred vertical displacement of the two edges, after removal of the intrinsic radial variations due to the eccentricity, along with the model fits. The fourth panel shows the overall radius residuals for the model, as a function of the phase angle θ . (Note that we do not show both fits in the same figure here, as the data points in the third panel shift slightly when the eccen-

tricity parameters change, and the residuals for the two fits differ significantly.)

The Cassini-only fit yields mean radii for the inner and outer edges, $a_{\text{in}} = 77,531.70 \pm 0.04$ km and $a_{\text{out}} = 77,532.23 \pm 0.05$ km, with radial amplitudes, $ae = 1.01 \pm 0.06$ km and 1.14 ± 0.07 km, respectively. The mean radial width of the gap is thus $\Delta a = 0.53 \pm 0.07$ km, very similar to the value of W_0 obtained from the simple gap model above. As expected, both pericenters are closely aligned with Titan, with $\phi_L = 0.3^\circ$ and 3.2° , respectively. With such similar eccentricities and aligned pericenters, it seems that we were justified above in assuming that the intrinsic radial width of the gap is essentially constant.

However, the vertical amplitudes of the two edges differ significantly, with that of the inner edge being much larger than that of the outer edge. Our best-fit values are $A_V^{\text{in}} = 3.79 \pm 0.10$ km and $A_V^{\text{out}} = 1.21 \pm 0.09$ km. Moreover, the phases of the two

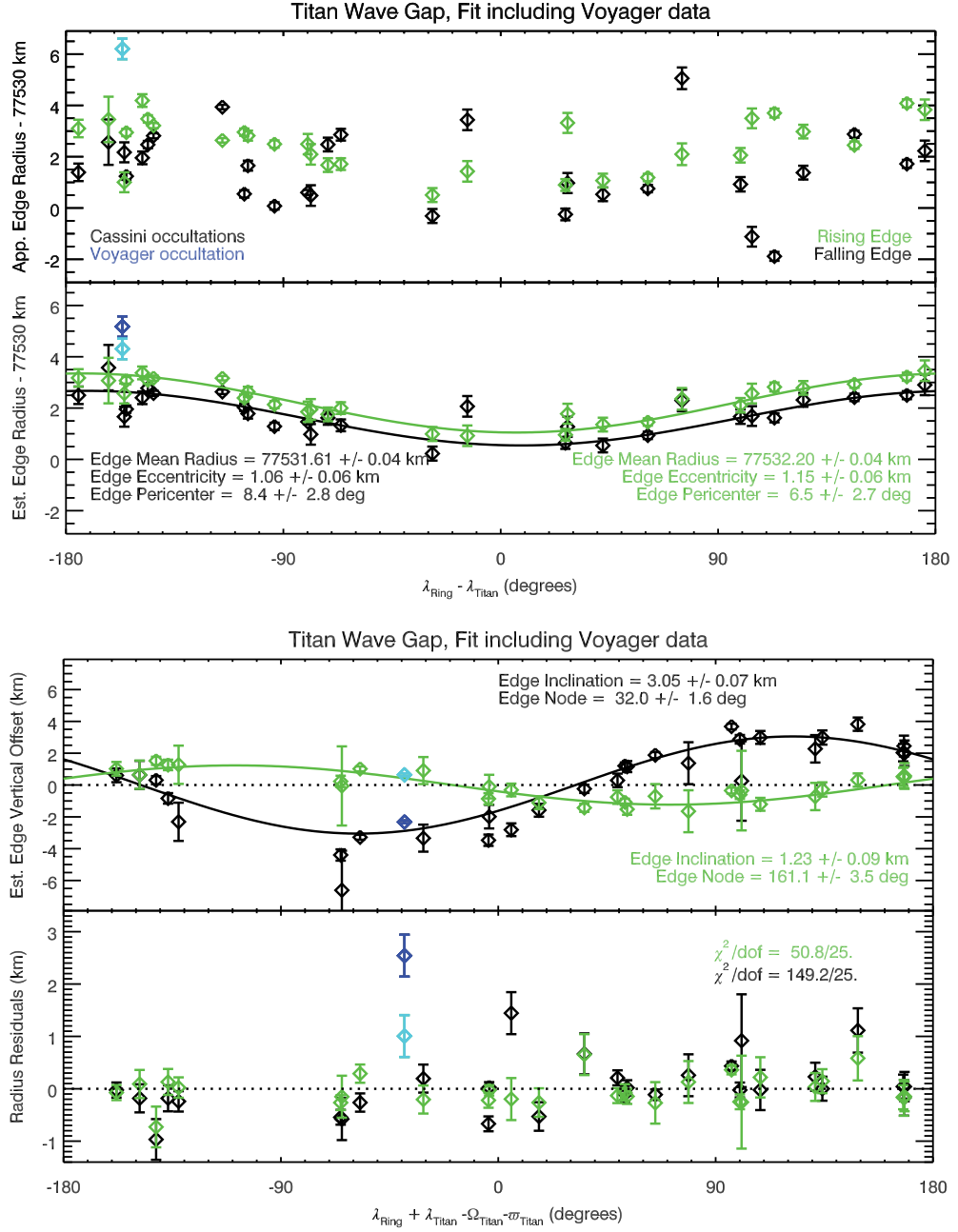


Fig. 8. Apparent radii and inferred radial and vertical displacements for both edges of the gap at 77,532 km. Layout is as in Fig. 7, but this fit includes the Voyager RSS points, which are again plotted in blue. The fitted amplitudes are now $A_V = 3.05 \pm 0.07$ km and 1.23 ± 0.09 km for the inner and outer edges, respectively, while the radial gap width is slightly greater at 0.59 ± 0.07 km. (Note that the Voyager RSS inner gap edge is off-scale in the upper panel, at -8 km.)

edges are significantly mis-aligned, with $\phi_V^{\text{in}} = 38.1 \pm 1.4^\circ$ and $\phi_V^{\text{out}} = 145.7 \pm 5.2^\circ$. Taking into account the difference of $\sim 108^\circ$ in the nodes, the differential vertical amplitude between the inner and outer edge (evaluated using the cosine theorem: $(\Delta A_V)^2 = (A_V^{\text{in}})^2 + (A_V^{\text{out}})^2 - 2A_V^{\text{in}}A_V^{\text{out}} \cos(\phi_V^{\text{out}} - \phi_V^{\text{in}})$) is $\Delta A_V \simeq 4.3$ km, in good agreement with the simple gap width model above.

The χ^2 values for these fits are 50.9 and 35.2, respectively, substantially higher than the 24 degrees of freedom in each fit. This probably indicates that our error bars on the absolute edge positions are underestimated by about 25%, likely due to small systematic errors in the geometry of the relevant occultations. Not surprisingly, the same data points that were most important in constraining the vertical gap amplitude in Fig. 5 act to establish the individual edge amplitudes in the present fit, while the α CMA 168

and 169 points lie very close to the longitudes where the inner and outer edges have the same vertical displacement.

However, our Cassini-only fits significantly overestimate the apparent width of the gap in the Voyager RSS data: the predicted width is 17.7 km, and the radius residuals for the inner and outer gap edges are 6.0 and 2.3 km, respectively. (*i.e.*, the measured gap width is $6.0 - 2.3 = 3.7$ km narrower than the model value.) When we include the Voyager RSS datum, the effects on the mean radii and eccentricities are negligible but, as in the case of the gap width fits in Fig. 5, the overall vertical amplitude is reduced. In this case, that of the outer edge is almost unchanged, but A_V^{in} is reduced from 3.79 km to 3.05 ± 0.07 km. The nodes of both edges also shift by $\sim 10^\circ$, with their separation increasing to $\Delta\phi_V \simeq 129^\circ$. The differential amplitude $\Delta A_V \simeq 3.6$ km, again in good agreement

Table 3
Summary of models for the gap in the Titan –1:0 bending wave.

	W_0 or a (km)	ae (km)	ϕ_L^a	$\text{asin } i$ (km)	ϕ_V^b	χ^2/dof
Apparent width:						
Cassini data only	0.59 ± 0.09	—	—	4.35 ± 0.23	$203 \pm 2^\circ$	14.2/26
Incl. Voyager datum	0.59 ± 0.09	—	—	3.71 ± 0.13	$199 \pm 2^\circ$	26.1/27
Inner edge, r_1 :						
Cassini data only	77531.70 ± 0.04	1.01 ± 0.06	$0 \pm 3^\circ$	3.79 ± 0.10	$38 \pm 2^\circ$	50.9/24
Incl. Voyager datum	77531.61 ± 0.04	1.06 ± 0.06	$8 \pm 3^\circ$	3.05 ± 0.07	$32 \pm 2^\circ$	149.2/25
Outer edge, r_2 :						
Cassini data only	77532.23 ± 0.05	1.14 ± 0.07	$3 \pm 3^\circ$	1.21 ± 0.09	$146 \pm 5^\circ$	35.2/24
Incl. Voyager datum	77532.20 ± 0.04	1.15 ± 0.06	$7 \pm 3^\circ$	1.23 ± 0.09	$161 \pm 4^\circ$	50.8/25

^a Pericenter measured relative to λ_T .

^b Node measured relative to $\Omega_T + \varpi_T - \lambda_T$.

with the simple gap width model in Fig. 5. However, the χ^2 values for these fits are substantially higher than those for the *Cassini*-only fits, especially for the inner edge. Inspection of Fig. 8 shows that several of the *Cassini* data show quite large residuals, especially compared with those for the same points in Fig. 7. Particularly notable are the residuals for 2 Cen 194e, α CMa 168 and 169 and β Peg 104. This might suggest that something is missing from the model (as noted above, one possibility is that the vertical amplitude of the gap edge perturbations has increased significantly since 1980). Another distinct possibility is that there are unidentified systematic errors in the geometry of the *Voyager* occultation that are magnified by its extreme viewing geometry.

For this reason, and because of its exceptionally wide gap, it is worth looking a little more closely at the *Voyager* RSS data. The model fit predicts vertical displacements of $z_{\text{in}} = -2.9$ km for the inner edge and $z_{\text{out}} = 0.4$ km for the outer edge. Using the amplification factor $\beta = -4.51$, and allowing for the intrinsic radial gap width of 0.6 km, the predicted radial width of the gap is $W = W_0 - \beta(z_{\text{out}} - z_{\text{in}}) = 15.6$ km. Radial residuals with respect to the combined edge model in Fig. 8 are 2.5 and 0.9 km for the inner and outer gap edges, respectively, much improved over those obtained for the *Cassini*-only fits. (i.e., the measured gap width of 14 km is now only $2.5 - 0.9 = 1.6$ km narrower than the model value.) However, our assumed radial uncertainty of 400 m for the *Voyager* RSS data in the C ring almost certainly underestimates the systematic uncertainty in the absolute radii, which is of order 1 km (Nicholson et al., 1990). We therefore consider the *Cassini*-only fits for the gap edges in Fig. 7 to be more reliable than the combined fits in Fig. 8. (A systematic error in the *Voyager* radius scale has no effect on the gap width, of course, or the combined fit in Fig. 5.)

The large predicted vertical displacement of the inner gap edge also explains why, in Fig. 4, the inner edge of the gap in the *Voyager* RSS data has an apparent radius that is so much less than that in any of the *Cassini* profiles.

All of our model fits are summarized in Table 3, using the model parameters from Figs. 5–8. The original uncertainties in the fit parameters shown in the figures have been retained here, but could easily be rescaled by a factor of $\sqrt{\chi^2/\text{dof}}$ to account for any perceived under- or overestimates of the errors in the data.

5. Discussion

Our investigation of the unusual structure near the inner edge of the Titan nodal bending wave has shown that this can be interpreted as a sub-kilometer-wide gap with edges that are inclined relative to one another with a maximum vertical displacement of ~4 km. This vertical distortion slowly revolves around Saturn in a retrograde direction, with a period close to that of Titan's orbital motion, consistent with forcing by the –1:0 inner vertical resonance. Separate fits to the inner and outer edges of the gap indicate that the vertical displacement is larger on the inner edge,

and that there is a phase shift of $\sim 110^\circ$ across the gap. The gap edges are also slightly eccentric, due to forcing by the nearby Titan 1:0 apsidal resonance. Fig. 9 provides a graphical illustration of our model for the gap and shows how it can appear from different vantage points either as a gap with variable width, or as a peak in optical depth when the two edges are viewed projected on top of each other.

This simple cartoon also suggests a possible explanation for the sharp maxima in optical depth seen on either side of the more prominent gaps in Figs. 2 and 3, as well as for the dips seen immediately on either side of the peaks. When the gap is seen at its widest, the stellar line of sight must penetrate the ring almost radially, and roughly parallel to the sloping upturned and down-turned edges of the gap. In such a geometry, the tangential path length through the rings is unusually high, leading to a maximum in τ_n , as observed. Conversely, when a prominent peak is observed, i.e., where the two edges overlap, the line of sight must penetrate the ring again almost radially, but at a steeper incidence angle to the edges of the gap, leading to minima in τ_n adjacent to the peak itself.

Although our kinematic models provide quite a good description of this unique feature, and connect it to the Titan –1:0 resonance, the exact nature of the relationship between the gap and the nodal bending wave in which it is embedded so far remains unclear. In their initial study of this structure, Rosen and Lissauer (1988) successfully modeled the wave's dispersion relation with the standard linear model of Shu (1984) and a spatially-varying background surface mass density that decreased from $\sigma_0 \simeq 0.9 \text{ g cm}^{-2}$ in the near-wave region to $\sim 0.4 \text{ g cm}^{-2}$ in the far-wave region. The average value of $\sigma_0 \simeq 0.65 \text{ g cm}^{-2}$ corresponds to a predicted vertical wave amplitude of ~ 400 m, via Eq. (15) above. This amplitude, however, was insufficient to account for the 'W-shaped' features observed in the innermost part of the *Voyager* RSS profile, which Rosen and Lissauer (1988) interpreted as being due to multiple crossings of the radio beam through the vertically-distorted ring plane. Instead, they obtained a better match to the RSS optical depth profile of this region with a vertical wave amplitude of ~ 1.6 km and a radial wavelength of ~ 20 km, corresponding to an implausibly-large surface density of $\sim 4.5 \text{ g cm}^{-2}$ (see their Fig. 2).

Using similar fits of the linear dispersion relation to several of our highest-SNR occultation profiles, we find that the wavelength in the near-wave region is given approximately by $2\pi/k \simeq 130/(r - a_{\text{res}})$, where all dimensional quantities are expressed in kiloms. From Eq. (14), this corresponds to a mean surface mass density of $\sigma_0 \simeq 0.62 \text{ g cm}^{-2}$, very similar to that obtained by Rosen and Lissauer (1988). (Our fits also yield a mean value of $a_{\text{res}} = 77,515$ km, which is 10 km less than the predicted location of the –1:0 resonance.) On the unproven (and perhaps dangerous) assumption that the background mass density is constant across the region of interest, the above expression provides a convenient local estimate



Fig. 9. A simplified illustration of our model for the Titan nodal bending wave and its associated gap, as seen from above Saturn's pole and at successively lower elevations. The vertical resonance is located at the inner edge of the disk, and the bending wave propagates outwards with a constant amplitude. The wave is interrupted by a narrow, circular gap, across which the wave phase changes by 180°. At normal incidence, the apparent width of the gap is unaffected by the wave, but at lower elevations one edge can block the other, leading to the apparent disappearance of the gap at some longitudes. Note that this model does not properly capture the varying optical depth in the wave, as the graphic assumes a warped, opaque ring illuminated from the side, or the radial variation in wavelength of a real bending wave.

for the wavelength in the near-wave region that we will make use of below.

With a vertical amplitude of 3.8 km, the inner edge of the gap is by far the most highly-inclined feature in the C ring, and one of only a handful of features anywhere in Saturn's rings whose heights above the mean ring plane exceed 1 km. Our results also suggest that the Titan nodal bending wave may be well into the nonlinear regime. The standard linear theory of bending waves, as described by Shu (1984), uses an approximate expression for the

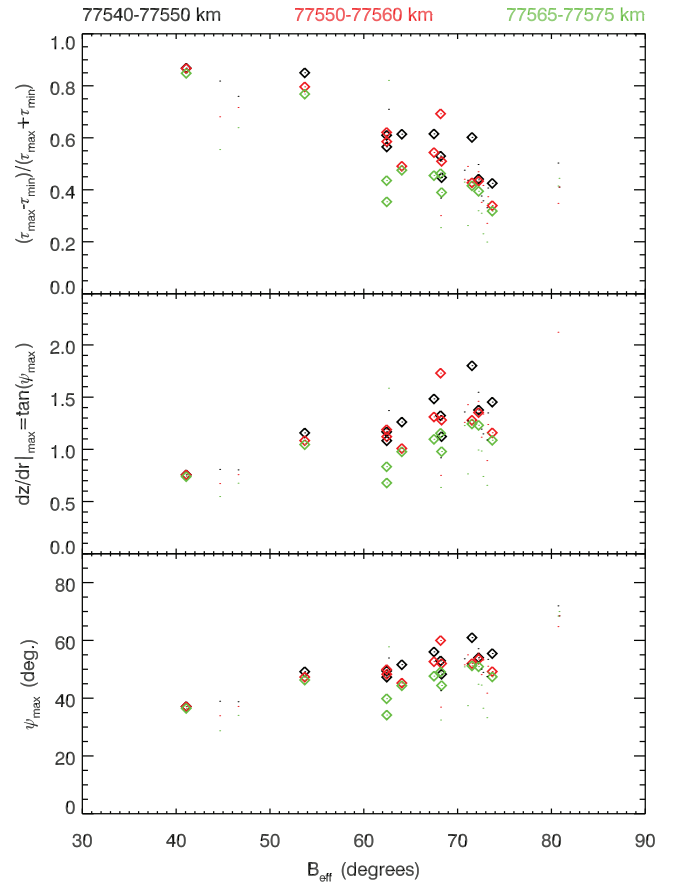


Fig. 10. Estimated maximum slopes for the bending wave in three radial regions, each 10 km wide, plotted as a function of B_{eff} . The top panel shows the measured range of apparent optical depths in each region, normalized by the average optical depth, while the middle panel shows the corresponding inferred maximum slopes, $\tan(\psi_{\max})$, using Eq. (22). In the bottom profile we plot ψ_{\max} itself. Data from only the highest-quality profiles are used here, in order to reduce unnecessary scatter. Note that, while the optical depth range decreases with increasing B_{eff} , the inferred slopes are fairly constant, as expected. The maximum slope does not appreciably diminish with increasing radius, although the wavelength (and therefore the amplitude of the wave) does.

gravitational field of the warped ring that allows the relevant perturbation to be expressed as a linear function of the vertical displacements (see Eqs. (68–70) of Shu (1984)). This approximation, however, is only valid if the maximum slope of the ring's surface, dz/dr is always much less than unity, and this assumption is strongly violated in the vicinity of the gap. The difference in the vertical positions of the gap edges can be as much as nine times their radial separation, and so the maximum value of dz/dr across the gap is ~ 9 ; it is likely, therefore, that the standard model of bending wave propagation breaks down in this region.

A closer examination of nearby regions in the Titan –1:0 bending wave indicates that the maximum radial slopes are actually quite high throughout the observable wave. For any quasi-sinusoidal corrugation, we can estimate the maximum slope of the ring, or equivalently the maximum slope angle ψ_{\max} , from the ratio of the maximum and minimum *apparent* normal optical depths using the expression (Hedman, 2007a):

$$\left(\frac{dz}{dr} \right)_{\max} = \tan(\psi_{\max}) = \tan B_{\text{eff}} \left(\frac{\tau_{\max} - \tau_{\min}}{\tau_{\max} + \tau_{\min}} \right). \quad (22)$$

Fig. 10 shows estimated values of the maximum slope for several different parts of the wave derived from the highest-SNR VIMS occultations, spanning both the near-wave and far-wave regions.

While there is some scatter in these measurements, the peak slopes in all three subregions of the wave are found to be around 50°, with $\tan \psi_{\max}$ being of order unity. While not nearly as large as that across the gap, these slopes are still high enough to violate the assumptions underlying the standard linear theory of bending waves.

It therefore appears that much of the Titan –1:0 bending wave could be effectively non-linear, with higher-order terms in the potential contributing significantly to the vertical accelerations of the ring material. Perhaps these extreme slopes could even be responsible for creating the gap in the first place. If the slope were to become much larger than unity, particles on nearby orbits could potentially be displaced vertically by more than the collisional mean free path. This could violate the standard assumption that the ring can be treated as a continuum sheet of material, and allow the ring to tear.

Combining the above notions with our estimates of the variable wavelength and maximum slope of the bending wave, we can put together a phenomenological description of this region that is more-or-less consistent with the observations, and that offers a possible explanation for the gap's existence.

- (1) From the WKB dispersion relation, Eq. (13), recast as Eq. (14), we find that the first wavelength of the bending wave is $\sim \sqrt{2} \times 130 \simeq 16$ km (see Eq. (18) of Nicholson et al., 2014a). The mean radius of the gap (77,532 km) is ~ 7 km from the expected resonance location and well within this first wavelength.
- (2) Taking our estimate for the vertical amplitude of the inner gap edge, $A_V = 3.8$ km, as indicative of the bending wave amplitude *interior to the gap*, we find a maximum slope in this region of $dz/dr = kA_V \simeq 1.3$, very similar to that found for the near-wave region exterior to the gap in Fig. 10. This amplitude is also compatible with what Rosen and Lissauer (1988) found necessary to fit the shapes of the W-shaped features in the RSS profile.
- (3) Immediately exterior to the gap, our model fits suggest a vertical amplitude $A_V = 1.2$ km. Again using the relation $(dz/dr)_{\max} = kA_V$ and an average wavelength at 77,545 km of ~ 6.5 km, we find that $\tan(\psi_{\max}) = 1.2$, consistent with the maximum slope observed in the 77,540–77,550 km region in Fig. 10.
- (4) Moving further outwards, we find from Fig. 10 that the maximum slope remains at $\tan(\psi_{\max}) \simeq 1.3$ in the 77,550–77,560 km region, where the mean wavelength is ~ 4.3 km. The corresponding vertical amplitude is only slightly smaller at ~ 0.9 km.
- (5) Outside $\sim 77,565$ km, the observed amplitude of the wave decreases abruptly (cf. Fig. 2), but from Fig. 10 we see that the maximum slope continues to saturate at ~ 1.1 . At 45 km from the resonance, the observed wavelength is ~ 2 km, implying a mean amplitude of only ~ 0.35 km.

Overall, we have a picture where, at each radius, the bending wave amplitude grows until it saturates at a maximum slope of $\sim 50^\circ$, or $dz/dr = kA_V \simeq 1.2$. The monotonic decrease in wavelength with distance from the resonance then requires that the vertical amplitude also decrease, from ~ 4 km at 7 km from a_{res} to ~ 1 km in the near-wave region and ~ 0.5 km at a distance of 45 km, in the far-wave region. We hypothesize that the slope first approaches unity during the bending wave's first wavelength, at ~ 7 km from the resonance. At this point, the rapidly-increasing amplitude results in the ring literally tearing itself apart vertically, as the local slope exceeds $\sim 50^\circ$. Immediately beyond this tear, the bending wave re-establishes itself – perhaps by tunneling across the narrow gap – but with a much reduced amplitude of ~ 1 km and a phase shift of 110° . The wave then continues to propagate outwards with

a fairly constant vertical amplitude (as predicted by the linear theory), until the slope again reaches the critical value. At this point, the amplitude begins to decrease, but is still ~ 0.9 km at 77,555 km, 30 km from the resonance. At 40 km from the resonance – perhaps because of an abrupt decrease in the background surface density, with a corresponding decrease in the wavelength – the slope again saturates and the amplitude is forced to drop to ~ 0.35 km.

In this context, we note that Gresh et al. (1986) concluded that the strong Mimas 5:3 bending wave in the outer A ring must also decrease in amplitude as it propagates, in order to match its profile in the Voyager RSS occultation data.

A wrinkle on the above picture is that, once the gap forms, the region between it and the resonant radius may become a type of resonant cavity, which could lead to a further enhancement of the wave amplitude in this region. A standing wave established in this region might account for the persistent optical depth minimum at $\sim 77,528$ km that we noted at the end of Section 3. A similar resonant cavity has been invoked to account for the substantial free normal modes seen at the outer edge of the B ring (Nicholson et al., 2014a; Spitale and Porco, 2010), and we would expect its width here to be one-quarter to one-half of the initial wavelength of the wave, or 4–8 km.

Finally, recall from the discussion of Figs. 2 and 3 in Section 3 that there is some evidence for an additional narrow gap/peak at a radius of $\sim 77,535$ km. This may well represent a second location where the slope becomes sufficiently steep for the ring to tear. Indeed, variations in the apparent width of this feature indicate that it can be explained by a model similar to that of the main gap, but with a much smaller vertical amplitude, perhaps less than 1 km.

A proper theoretical investigation of this wave is beyond the scope of this work, and probably beyond the existing linear theory for bending waves, but we hope to pursue this subject further in a future paper. In the future, we also hope to be able to incorporate other Cassini occultation datasets in our gap model, in particular several of the radio occultations that probed the C ring at opening angles of only a few degrees. Images taken by the Imaging Science Subsystem (ISS) near the time of equinox, when the Sun shone obliquely across the rings, may also be of considerable value in establishing the true vertical amplitude of the –1:0 bending wave.

Acknowledgments

This work was supported by NASA, through a grant to PDN from the Cassini Project. We acknowledge the efforts of the Cassini VIMS engineering and science teams in making the acquisition of these data possible, and the PDS Rings Node for providing the Voyager RSS profile in digital form. R.G French kindly provided an up-to-date list of spacecraft trajectory corrections based on his own unpublished analysis of the ring occultation data. Our discussion of the residuals in our fits greatly benefitted from comments by an anonymous reviewer. A preliminary version of this study was presented at the 2010 DPS meeting in Fajardo, PR.

Appendix

In Figs. 11–16 we present optical depth profiles of the gap region for all of the occultations we have analyzed here, including the Voyager RSS data extracted from the PDS Rings Node. In each panel we also show the measured radii of the inner and outer gap edges, as used in the model fits in Figs. 7 and 8. The actual radii, r_1 and r_2 , as well as all relevant geometrical parameters, may be found in Table 1.

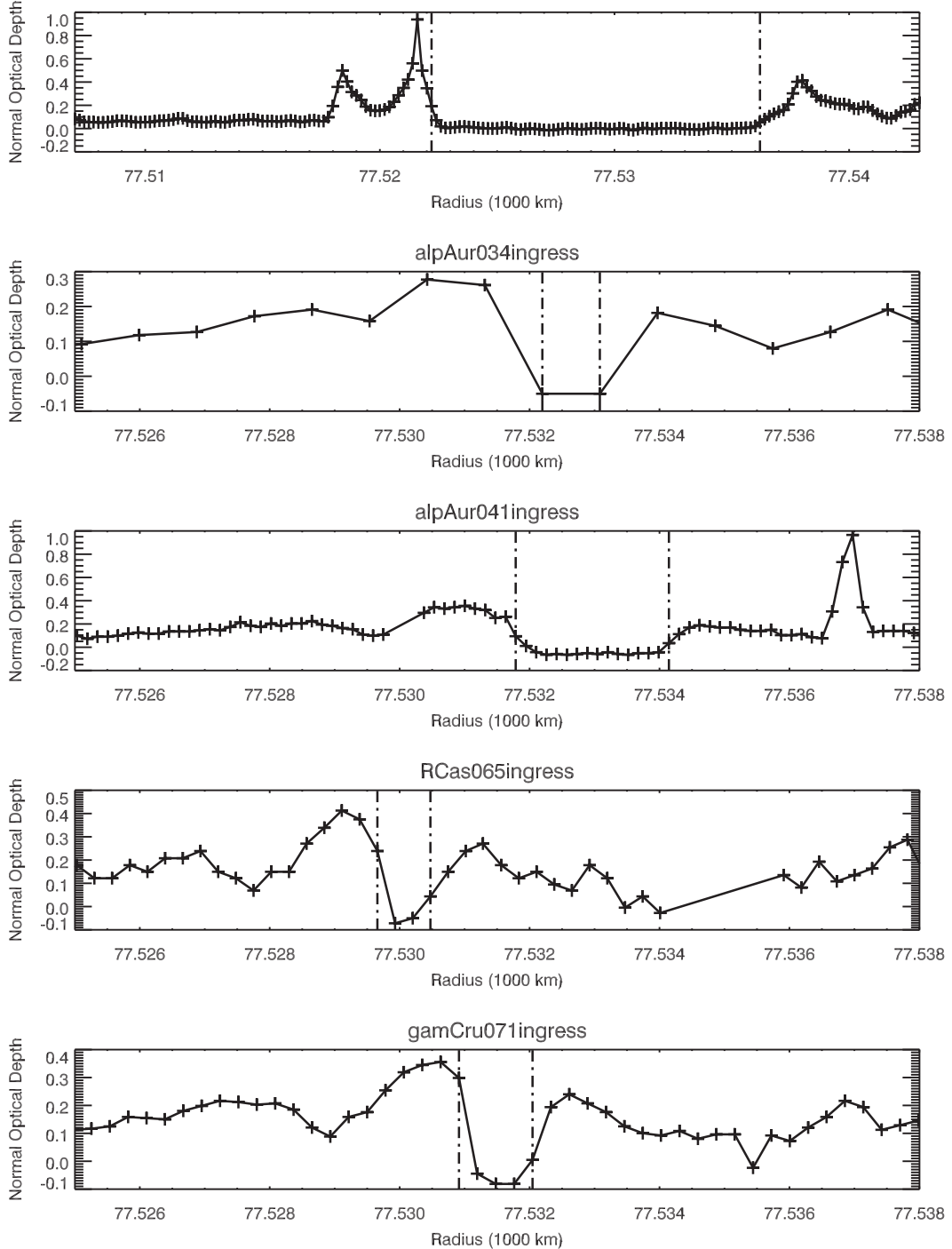


Fig. 11. The complete set of occultation profiles analyzed in this work for the region of the gap seen in the Titan –1:0 bending wave. The measured positions of the inner and outer gap edges are indicated by vertical dot-dashed lines. These radii provide the input to the least-squares fits shown in Figs. 5, 7 and 8. Plus signs indicate individual occultation measurements, acquired at intervals of 20 to 80 ms. Short data gaps in some profiles (e.g., R Cas 65) indicate pauses due to instrumental background measurements. The first profile is from the Voyager RSS occultation, while the remainder are from Cassini VIMS stellar occultations, as labeled above each panel. Except for the RSS profile, all plots are on a common radius scale.

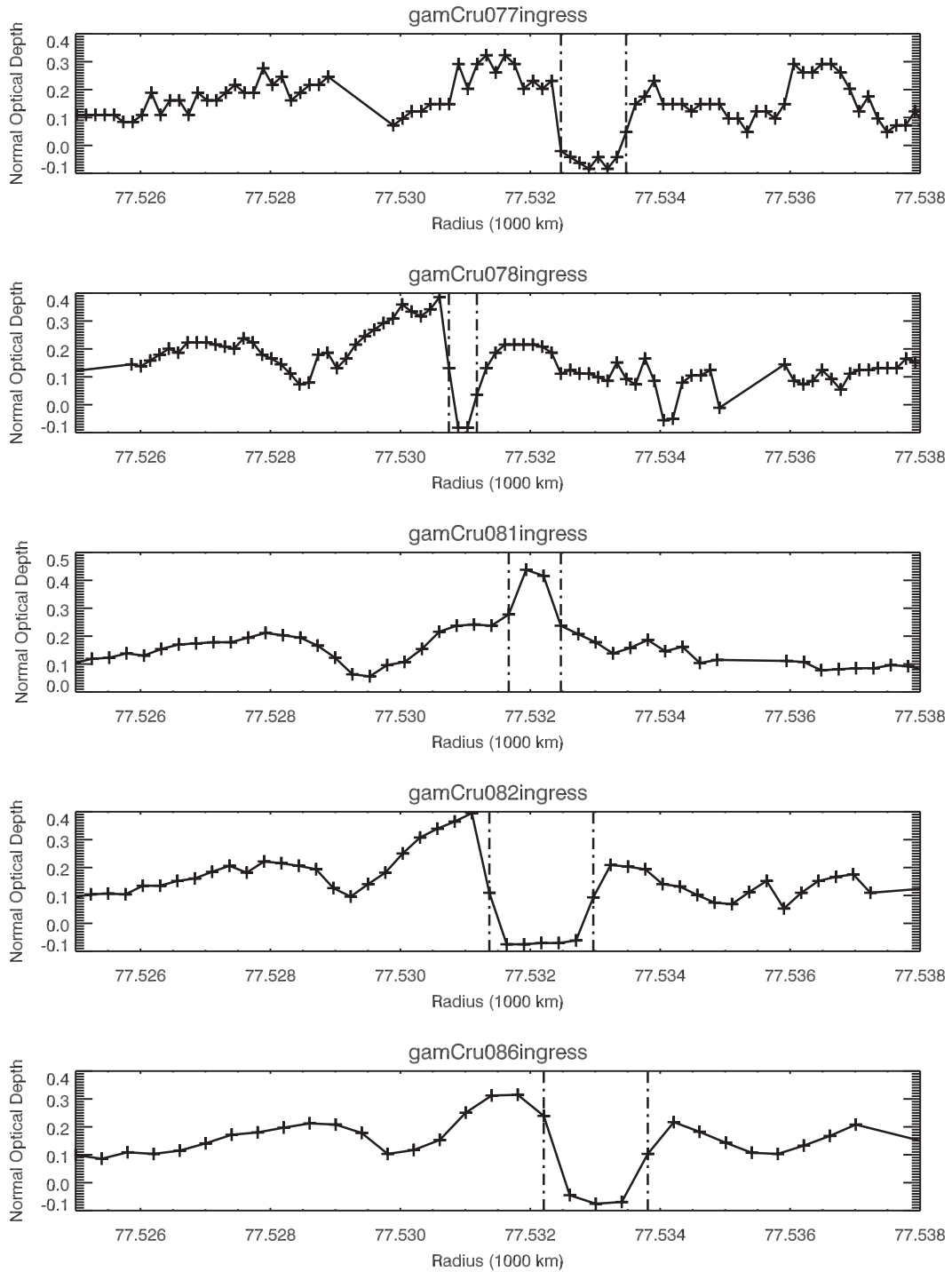
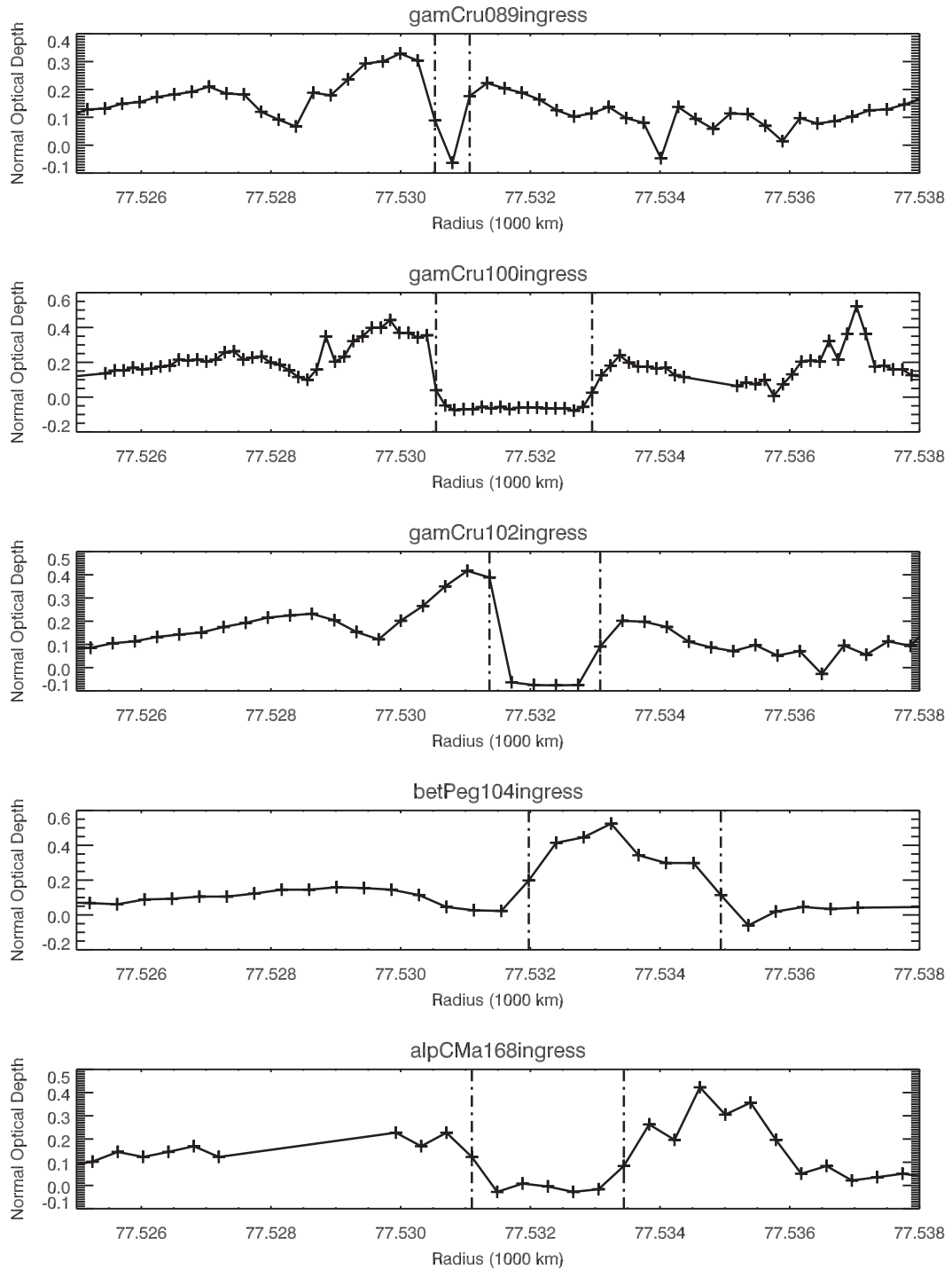


Fig. 12. Continued from Fig. 11.

**Fig. 13.** Continued from Fig. 11.

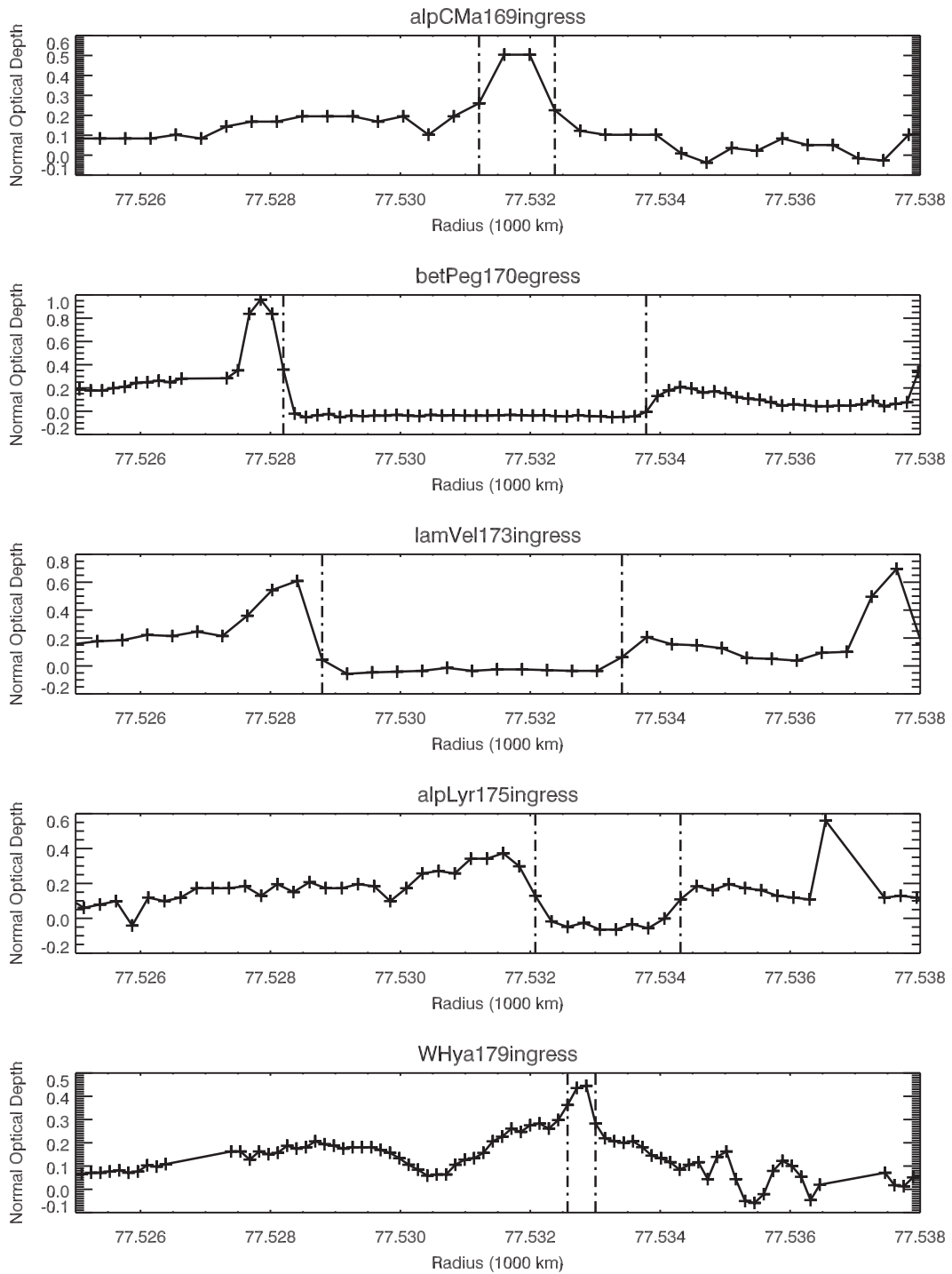
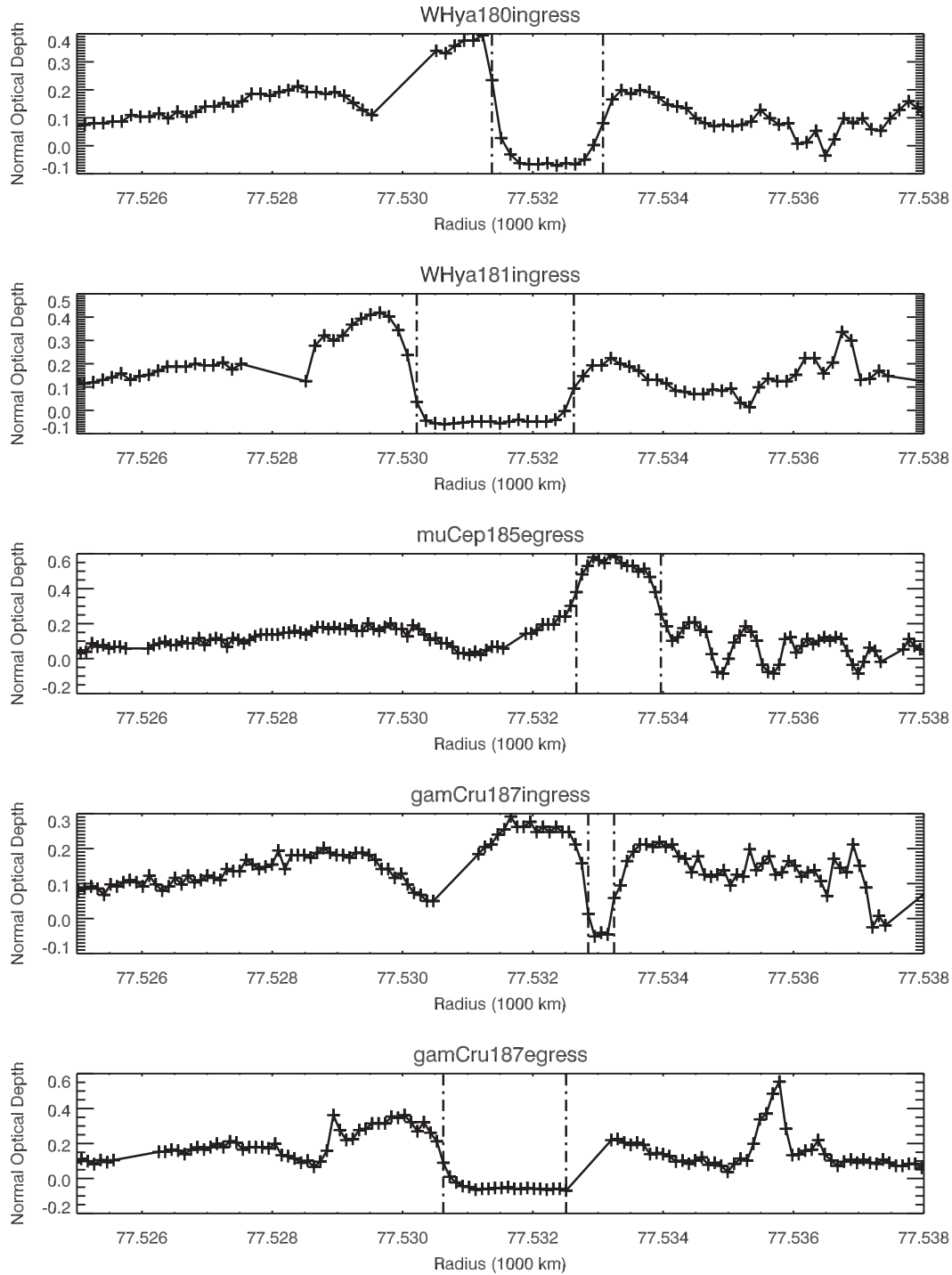


Fig. 14. Continued from Fig. 11.

**Fig. 15.** Continued from Fig. 11.

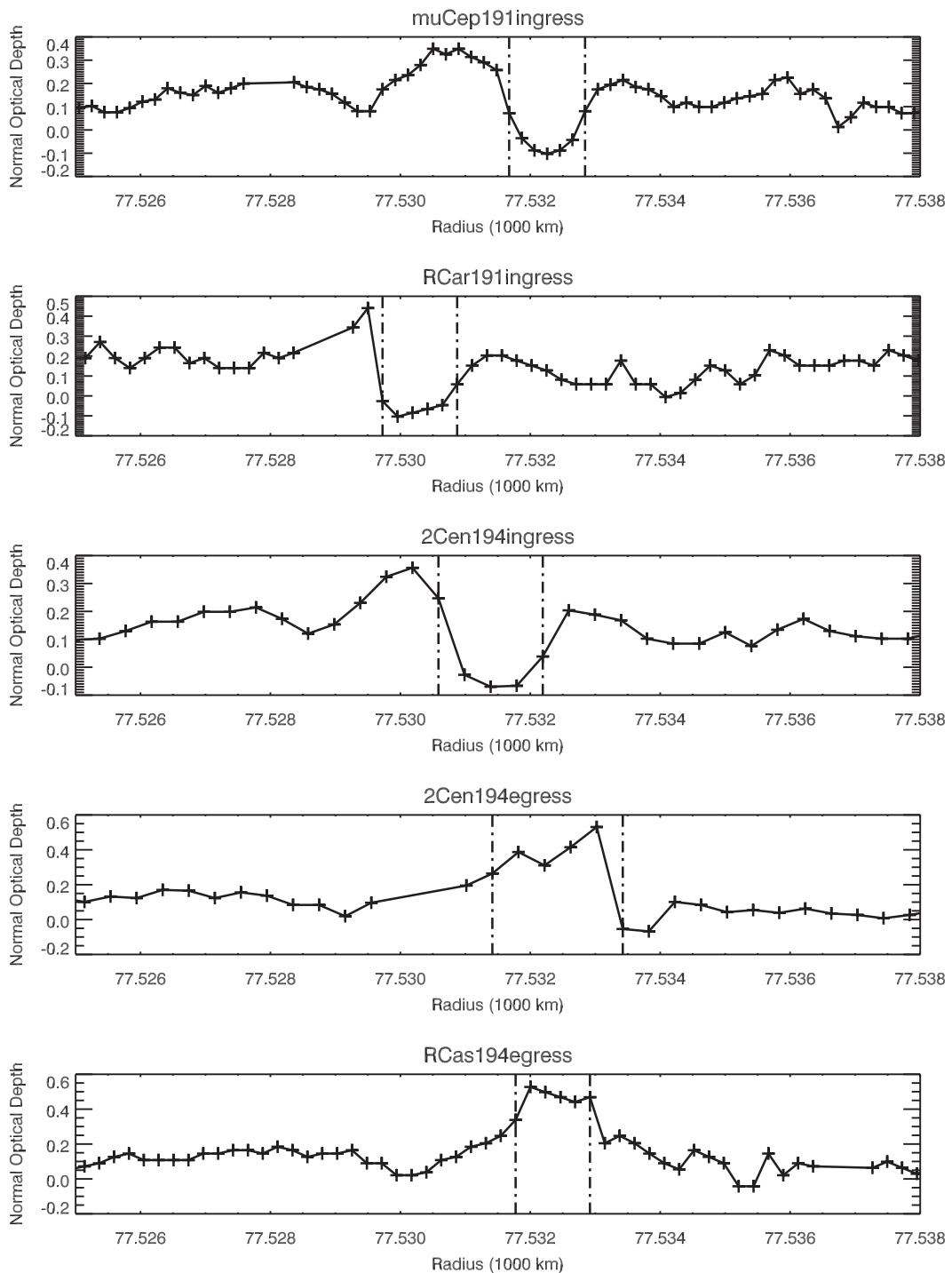


Fig. 16. Continued from Fig. 11.

References

- Baillié, K., Colwell, J.E., Lissauer, J.J., et al., 2011. Waves in Cassini UVIS stellar occultations. 2. The C ring. *Icarus* 216, 292–308.
- Brown, R.H., Baines, K.H., Bellucci, G., et al., 2004. The Cassini visual and infrared mapping spectrometer (VIMS) investigation. *Space Sci. Rev.* 115, 111–168.
- Cuzzi, J.N., Lissauer, J.J., Shu, F.H., 1981. Density waves in Saturn's rings. *Nature* 292, 703–707.
- ESA, 1997. The Hipparcos and Tycho Catalogues. VizieR Online Data Catalog 1239, 0.
- Gresh, D.L., Rosen, P.A., Tyler, G.L., et al., 1986. An analysis of bending waves in Saturn's rings using Voyager radio occultation data. *Icarus* 68, 481–502.
- Hedman, M.M., Burns, J.A., Showalter, M.R., et al., 2007a. Saturn's dynamic D ring. *Icarus* 188, 89–107.
- Hedman, M.M., Nicholson, P.D., 2013. Kronoseismology: Using density waves in Saturn's C ring to probe the planet's interior. *Astron. J.* 146, 12.
- Hedman, M.M., Nicholson, P.D., 2014. More kronoseismology with Saturn's rings. *Mon. Not. R. Astron. Soc.* 444, 1369–1388.
- Hedman, M.M., Nicholson, P.D., Salo, H., et al., 2007b. Self-gravity wake structures in Saturn's A ring revealed by Cassini VIMS. *Astron. J.* 133, 2624–2629.
- Jacobson, R.A., et al., 2008. The gravity field of the Saturnian system and the orbits of the major Saturnian satellites. In: Paper presented at "Saturn after Cassini-Huygens" symposium. Imperial College, London.
- Jacobson, R.A., French, R.G., Hedman, M., et al., 2011. The pole orientation, pole precession, and moment of inertia factor of Saturn. *EPSC-DPS Jt. Meet.* 2011, 1070.
- Jerousek, R.G., Colwell, J.E., Esposito, L.W., 2011. Morphology and variability of the Titan ringlet and Huygens ringlet edges. *Icarus* 216, 280–291.

- Lissauer, J.J., 1985. Bending waves and the structure of Saturn's rings. *Icarus* 62, 433–447.
- Markwardt, C.B., 2009. Non-linear least squares fitting in IDL with MPFIT. *Astron. Data Anal. Softw. Syst.* XVIII 411, 251.
- Murray, C.D., Dermott, S.F., 1999. *Solar System Dynamics*. (Cambridge University Press).
- Nicholson, P.D., Cooke, M.L., Pelton, E., 1990. An absolute radius scale for Saturn's rings. *Astron. J.* 100, 1339–1362.
- Nicholson, P.D., French, R.G., Hedman, M.M., et al., 2014a. Noncircular features in Saturn's rings: I the edge of the B ring. *Icarus* 227, 152–175.
- Nicholson, P.D., French, R.G., McGhee-French, C.A., et al., 2014b. Noncircular features in Saturn's rings: II the C ring. *Icarus* 241, 373–396.
- Nicholson, P.D., Hedman, M.M., 2010. Self-gravity wake parameters in Saturn's A and B rings. *Icarus* 206, 410–423.
- Nicholson, P.D., Porco, C.C., 1988. A new constraint on Saturn's zonal gravity harmonics from Voyager observations of an eccentric ringlet. *J. Geophys. Res.* 93, 10209–10224.
- Porco, C., Nicholson, P.D., Borderies, N., et al., 1984. The eccentric Saturnian ringlets at 1.29 R_s and 1.45 R_s . *Icarus* 60, 1–16.
- Rosen, P.A., Lissauer, J.J., 1988. The Titan-1:0 nodal bending wave in Saturn's ring C. *Science* 241, 690–694.
- Shu, F.H., 1984. Waves in planetary rings. In: Brahic, A., Greenberg, R. (Eds.), *Planetary Rings*. University of Arizona Press, pp. 513–561.
- Spitale, J.N., Porco, C.C., 2010. Detection of free unstable modes and massive bodies in Saturn's outer B ring. *Astron. J.* 140, 1747–1757.
- Tiscareno, M.S., Hedman, M.M., Burns, J.A., et al., 2013. Probing the inner boundaries of Saturn's A ring with the Iapetus -1:0 nodal bending wave. *Icarus* 224, 201–208.